SPECIAL
Oceanic Flow—Topography Interactions
COLLECTION

Energetic Stratified Turbulence Generated by Kuroshio–Seamount Interactions in Tokara Strait

ANNE TAKAHASHI,[a] REN-CHIEH LIEN,[a] ERIC KUNZE,[b] BARRY MA,[a] HIROHIKO NAKAMURA,[c] AYAKO NISHINA,[c] EISUKE TSUTSUMI,[c,d] RYUICHIRO INOUE,[e] TAKEYOSHI NAGAI,[f] AND TAKAHIRO ENDOH[g]

[a] *Applied Physics Laboratory, University of Washington, Seattle, Washington*
[b] *NorthWest Research Associates, Redmond, Washington*
[c] *Faculty of Fisheries, Kagoshima University, Kagoshima, Japan*
[d] *Atmosphere and Ocean Research Institute, The University of Tokyo, Tokyo, Japan*
[e] *Research Institute for Global Change, Japan Agency for Marine-Earth Science and Technology, Yokosuka, Japan*
[f] *Department of Ocean Sciences, Tokyo University of Marine Science and Technology, Tokyo, Japan*
[g] *Research Institute for Applied Mechanics Kyushu University, Fukuoka, Japan*

(Manuscript received 30 November 2022, in final form 14 November 2023, accepted 28 November 2023)

ABSTRACT: Generating mechanisms and parameterizations for enhanced turbulence in the wake of a seamount in the path of the Kuroshio are investigated. Full-depth profiles of finescale temperature, salinity, horizontal velocity, and microscale thermal-variance dissipation rate up- and downstream of the ~10-km-wide seamount were measured with EM-APEX profiling floats and ADCP moorings. Energetic turbulent kinetic energy dissipation rates $\varepsilon \sim \mathcal{O}(10^{-7}\text{–}10^{-6})$ W kg^{-1} and diapycnal diffusivities $K \sim \mathcal{O}(10^{-2})$ m^2 s^{-1} above the seamount flanks extend at least 20 km downstream. This extended turbulent wake length is inconsistent with isotropic turbulence, which is expected to decay in less than 100 m based on turbulence decay time of $N^{-1} \sim 100$ s and the 0.5 m s^{-1} Kuroshio flow speed. Thus, the turbulent wake must be maintained by continuous replenishment which might arise from (i) nonlinear instability of a marginally unstable vortex wake, (ii) anisotropic stratified turbulence with expected downstream decay scales of 10–100 km, and/or (iii) lee-wave critical-layer trapping at the base of the Kuroshio. Three turbulence parameterizations operating on different scales, (i) finescale, (ii) large-eddy, and (iii) reduced-shear, are tested. Average ε vertical profiles are well reproduced by all three parameterizations. Vertical wavenumber spectra for shear and strain are saturated over 10–100 m vertical wavelengths comparable to water depth with spectral levels independent of ε and spectral slopes of -1, indicating that the wake flows are strongly nonlinear. In contrast, vertical divergence spectral levels increase with ε.

KEYWORDS: Instability; Internal waves; Turbulence; In situ oceanic observations

1. Introduction

When ocean currents interact with topography, the energy of large-scale flow cascades to smaller scales to enhance turbulent dissipation of balanced, tidal, and internal-wave energy, as well as mixing of water properties. These interactions include critical reflection (Eriksen 1982, 1998) and scattering of internal waves (Müller and Xu 1992), internal tide generation (e.g., Garrett and Kunze 2007; Klymak et al. 2008), mean-flow generation of lee waves (e.g., Bell 1975a,b; Naveira Garabato et al. 2004; Nikurashin and Ferrari 2010; Waterman et al. 2013; Legg 2021), hydraulically controlled flow (Farmer and Armi 1999; Klymak and Gregg 2004), and vortex wakes (e.g., Baines 1995; Chang et al. 2013; MacKinnon et al. 2019; Nagai et al. 2021) and so may be important sinks for ocean energy budgets (e.g., Wunsch and Ferrari 2004).

Flow–topography interaction physics varies with flow speed U and frequency ω, stratification N, Earth's rotation f, and topographic horizontal L and vertical H length scales (Baines 1995; Garrett and Kunze 2007). If topography has small dynamical aspect ratios $NH/(fL)$, interaction with geostrophic and tidal currents can be described analytically with linear lee-wave or internal tide generation theories (Bell 1975a,b). Interactions become nonlinear as topography steepens (e.g., Kunze and Toole 1997; St. Laurent et al. 2003; Nikurashin et al. 2014). Stratified flow is blocked or split around tall topography (Baines 1995), exciting a submesoscale vortex wake (e.g., Chang et al. 2013; Caldeira et al. 2014; Perfect et al. 2018, 2020a; MacKinnon et al. 2019; Johnston et al. 2019) as well as lee waves (e.g., Nikurashin et al. 2014; Johnston et al. 2019; Perfect et al. 2020b). Waves and eddies of large amplitude and wavenumber will induce hydraulic jumps and

---

Denotes content that is immediately available upon publication as open access.

Corresponding author: Anne Takahashi, annetaka@uw.edu

DOI: 10.1175/JPO-D-22-0242.1

instabilities, resulting in enhanced turbulent dissipation and mixing (e.g., Thorpe 1992; Polzin et al. 1997; Kunze and Toole 1997; Toole et al. 1997; Moum and Nash 2000; Kunze et al. 2002; Nash et al. 2004; Klymak et al. 2008; Kunze et al. 2012).

The Kuroshio, which is the major western boundary current of the wind-driven North Pacific subtropical gyre, flows through regions of rapidly changing complex topography. Previous microstructure measurements in Tokara Strait, where the Kuroshio interacts with islands and seamounts, have found turbulent kinetic energy (TKE) dissipation rates ε exceeding 10^{-7} W kg^{-1} and diapycnal diffusivities K exceeding 10^{-4} m^2 s^{-1} that extend at least 100 km downstream of seamounts (Tsutsumi et al. 2017; Nagai et al. 2017, 2019, 2021; Hasegawa et al. 2021). Some of these elevated dissipation rates were associated with

- high-vertical-wavenumber shear along isopycnals suggestive of near-inertial waves (Nagai et al. 2019, 2021),
- negative potential vorticity, suggesting inertial-symmetric instabilities (Nagai et al. 2021),
- Kelvin–Helmholtz (KH) instabilities (Hasegawa et al. 2021), and
- bottom-boundary layer separation (Hasegawa et al. 2021),

all presumably resulting from flow–topography interactions. Downstream energetic turbulence will induce vertical mixing and inject subsurface nutrient-rich waters (Guo et al. 2012, 2013) into the sunlit surface layer (Nagai et al. 2019; Hasegawa et al. 2021) which will impact phytoplankton growth and CO$_2$ uptake (Takahashi et al. 2009).

Strong Kuroshio–topography interactions have also been observed near Green Island, Taiwan, where TKE dissipation rates are estimated to be $\mathcal{O}(10^{-7}$–$10^{-4})$ W kg^{-1} (Chang et al. 2013, 2016, 2019). Assuming that energetic turbulence extends along the Kuroshio between Taiwan and Tokara Strait, the overall dissipation is estimated to be $\rho\varepsilon DxDyDz \sim 10^9$ W, where seawater density $\rho \sim 10^3$ kg m^{-3}, TKE dissipation rate $\varepsilon \sim \mathcal{O}(10^{-6})$ W kg^{-1}, along-stream $Dx \sim 3$–4×10^5 m, across-stream $Dy \sim 3$–4×10^4 m and vertical $Dz \sim 2 \times 10^2$ m in the turbulent layer. This value is comparable to the $\sim 10^{10}$ W wind-work on the North Pacific subtropical gyre (Scott and Xu 2009). While likely an overestimate, it does not account for additional interactions with topography south of Taiwan or north of Tokara Strait, suggesting that Kuroshio interactions with topography may be an important sink for the subtropical wind-forced gyre-scale circulation.

Large topographic dynamical aspect ratios $NH/(fL)$ at seamounts in Tokara Strait suggest nonlinear flow–topography interactions where geostrophic and tidal currents generate internal waves and submesoscale vortices with overlapping time and length scales (MacKinnon et al. 2019; Johnston et al. 2019; Perfect et al. 2020a,b; Puthan et al. 2021). These fluctuations can interact with each other to become nonlinear and unstable to turbulent production and dissipation. Nonlinearities complicate the interpretation of finescale flow fields, and fine- and microscale cannot be reproduced simultaneously in simulations. Thus, our understanding of the physical processes generating energetic turbulence at seamounts, that is, processes connecting finescale and microscale, is still uncertain.

Microstructure measurements of turbulence are generally time-consuming, so various parameterizations have been proposed to quantify the variability of turbulent mixing using more readily available finescale variables. Among them, the finescale parameterization (e.g., Gregg 1989; Polzin et al. 1995) has been widely validated in the interior ocean (e.g., Hibiya et al. 2012; Whalen et al. 2015) and applied (e.g., Whalen et al. 2012; Kunze 2017). However, the finescale parameterization is not expected to be valid where the dominant turbulent production physics is distinct from weakly nonlinear wave–wave interactions (McComas and Müller 1981; Henyey et al. 1986), such as bottom boundary layers (Carter and Gregg 2002; MacKinnon and Gregg 2005; Polzin et al. 2014a,b), wave–mean flow interactions (Waterman et al. 2014; Kunze and Lien 2019; Wu et al. 2023), and direct breaking of internal tides near topography (Klymak et al. 2008). In energetic internal waves, low modes can become unstable and generate turbulence (D'Asaro and Lien 2000b; MacKinnon and Gregg 2005) so that the large-eddy parameterization (Moum 1996) may be more appropriate than the finescale parameterization. Shear-driven turbulence can also be estimated using the reduced-shear parameterization (Kunze et al. 1990) if unstable shear layers with gradient Richardson numbers less than 0.25 are resolved.

In this study, electromagnetic autonomous profiling explorer (EM-APEX) profiling float and acoustic Doppler current profiler (ADCP) mooring measurements in the vicinity of Hirase Seamount in Tokara Strait are used to address two scientific questions:

- How are velocity and density fine structure modified by flow–topography interactions?
- Which turbulence parameterizations are appropriate in the strongly nonlinear flow field?

The remainder of this paper is organized as follows. An overview of the measurements and data analysis methods is provided in section 2. In section 3, the dynamical flow–topography regime is discussed based on nondimensional parameters calculated from the bathymetry of Hirase, background flow, and stratification. In section 4, characteristics of the finescale horizontal velocity and density fields around Hirase are described. In section 5, strong turbulent layers extending for $\mathcal{O}(10)$ km downstream of the seamount are revealed by the EM-APEX float microstructure profiles. Possible causes for the enhanced turbulence are discussed. In section 6, vertical wavenumber spectra of vertical shear $\mathbf{v}_z$, strain η_z, and vertical divergence w_z are compared with the Garrett–Munk (GM) internal wave (Garrett and Munk 1975; Cairns and Williams 1976; Gregg and Kunze 1991; Thurnherr et al. 2015), isotropic turbulence (Kolmogorov 1941; Batchelor 1953; Ozmidov 1965; Tennekes and Lumley 1972; Thorpe 2005), and anisotropic turbulence (Kunze 2019) models. Then, in section 7, parameterizations for turbulence production based on finescale weak wave–wave interactions (Gregg 1989; Polzin et al. 1995), large-eddy turbulence (Moum 1996; D'Asaro and Lien 2000b), and reduced

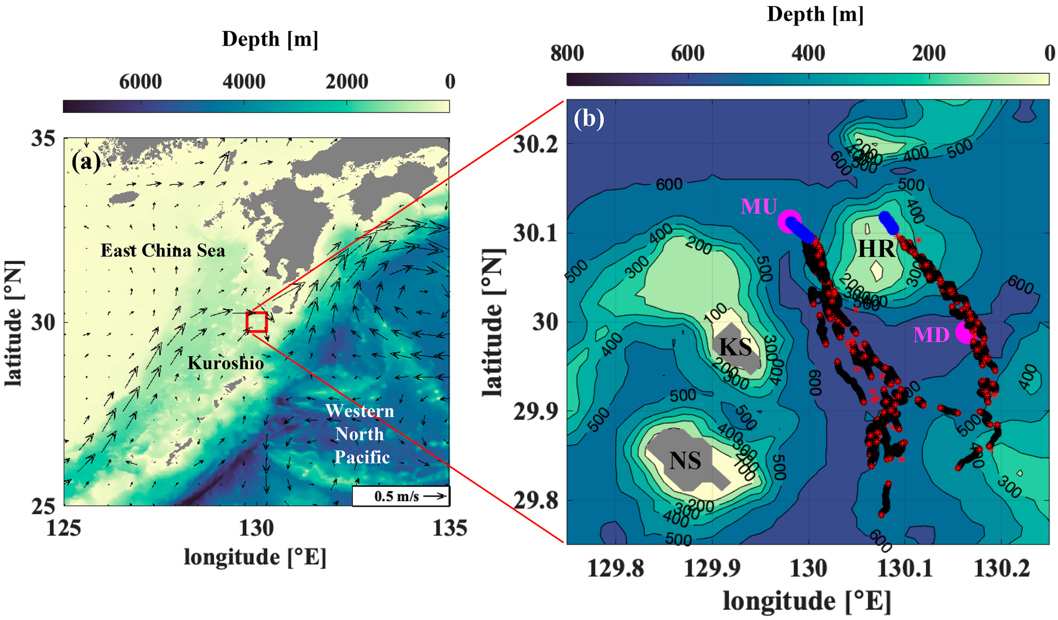

FIG. 1. (a) Bathymetry in the East China Sea and western North Pacific overlain with monthly mean horizontal current vectors at 5-m depth during November 2019 reveal the Kuroshio passing through the measurement site (small red box) in Tokara Strait. (b) Measurement site showing Hirase (HR), Kuchinoshima (KS), and Nakanoshima (NS). Magenta dots mark upstream (MU) and downstream (MD) mooring locations, blue dots are EM-APEX float deployment points, red asterisks are float descents and surfacings, and black lines are float trajectories for the western and eastern line-array deployments. Bathymetry is from ETOPO1, and horizontal currents in (a) are from the Copernicus Marine Environment Monitoring Service (CMEMS) Global Ocean Physics Reanalysis data.

shear (Kunze et al. 1990) are tested in the energetic fine structure downstream of Hirase. A summary and concluding remarks are given in section 8.

2. Data and methods

During November 2019, fine- and microstructure measurements were collected in Tokara Strait (30°N, Coriolis frequency $f = 7.3 \times 10^{-5}$ s^{-1}) to study interactions of the Kuroshio with Hirase Seamount (Fig. 1). Hirase is a ~400-m-tall, ~10-km-diameter flat-top bank in ~600-m-deep waters. The Kuroshio flowed southeastward with the surface speed of ~1 m s^{-1} throughout the measurement period.

Two moorings, each equipped with an upward-looking 75-kHz Teledyne RDI Long Ranger ADCP, were deployed upstream (MU) and downstream (MD) of the seamount (Fig. 1b). The moorings were deployed on 16–17 November and recovered on 21 November. Horizontal velocities (u, v) were measured every 30 s in 4-m vertical bins over depths of 50–550 m. The original horizontal velocity time series are smoothed over 10 min to reduce noise. Poor-quality velocity data with large velocity errors (>0.1 m s^{-1}) or low "Percent Good 4" values (PG4 < 90; a measure of the percentage of good-quality velocity data acquired with four ADCP beams) are also removed.

EM-APEX profiling floats were deployed in 10-float along-streamline arrays upstream of the seamount, one array on 17 November 2019 with trajectories west of Hirase and a second on 20 November 2019 with trajectories east of Hirase (Fig. 1b). Each line array was in the water for roughly 24 h while it was advected downstream of the seamount by the Kuroshio before recovery. Positions were tracked by GPS when the floats were at the surface. The float line arrays had horizontal resolution of $\mathcal{O}(100)$ m along their trajectories.

Each float was instrumented with two pairs of electromagnetic (EM) velocity sensors, dual fast-response FP07 thermistors, and a SeaBird Electronics SBE41 CTD (Sanford et al. 2005; Lien et al. 2016). The floats were programmed to profile continuously at a vertical speed of ~0.15 m s^{-1} between the sea surface and bottom while measuring temperature T, salinity S, pressure P, and horizontal velocity (u, v). Microscale thermal-variance dissipation rates χ were only measured during ascent.

a. Horizontal velocity

Float EM velocity sensors measure voltage differences across the instrument due to the electric field induced by conducting seawater moving in Earth's magnetic field (Sanford et al. 1978, 2005). Measured voltages are fit to a sinusoid over half-overlapping 50-s segments to estimate horizontal velocity in ~3.75-m depth intervals, producing independent horizontal velocities every ~7.5 m (Lien and Sanford 2019). Horizontal velocity (u, v) typically has less than 0.01 m s^{-1} uncertainty, and is relative to an unknown depth-independent constant which can vary with time and location. To obtain absolute horizontal velocity, the depth-independent constant is inferred by subtracting time-depth averaged float relative velocity from the velocity inferred from float GPS positions (Lien and Sanford 2019).

b. Vertical velocity

Vertical water velocity w is estimated as the difference between float's vertical profiling speed $w_m = -dp/dt$ and its theoretical profiling speed w_s

$$w = w_m - w_s \tag{1}$$

(Frajka-Williams et al. 2011; Cusack et al. 2017). In still water, float vertical motion is assumed to obey the equation of motion

$$M\frac{dw_s}{dt} = g(\rho V - M) - \rho C_D A |w_s| w_s \tag{2}$$

with float mass M, gravitational acceleration g, water density ρ, float volume V, float cross-sectional area A, and a nondimensional drag coefficient C_D. Assuming steady state where the buoyancy force is balanced by drag, vertical velocity is

$$w_s = \mathrm{sign}(\rho V - M)\sqrt{\frac{|g(M - \rho V)|}{\rho C_D A}}. \tag{3}$$

Float volume V is assumed to change linearly with water pressure P as well as with the position k of a piston at the bottom of the float, which is adjusted automatically to control ascent and descent speed,

$$V = V_0[1 + \alpha_P(P - P_0)] + \alpha_k(k - k_0), \tag{4}$$

where the unknown volume V_0 and piston position $k_0 = 42$ are referenced to $P_0 = 800$ dbar. Float compressibility coefficients α_P and α_k represent average values over the float because different components have different compressibilities.

Model equations (3) and (4) for w_s contain four unknowns, $C_D^* = C_D A$, V_0, α_P, and α_k, which are optimized by minimizing the cost function

$$\sum_t w^2(t) \tag{5}$$

over many profiles. Frajka-Williams et al. (2011) tried several possible cost functions and found (5) provides reasonable estimates. However, estimates could be biased when assumptions are violated; for example, if there is net up- or downwelling during the whole profile time series. In our data, theoretical profiling speed w_s tends to be smooth compared to w_m, so high-frequency (or high vertical wavenumber) w fluctuations, which are the main focus of this study, are not affected by details of the cost function. Optimization is performed for each float's deployment. Fit parameters are consistent with Cusack et al. (2017). Inferred vertical velocity w profiles have vertical resolution ~3 m, and are gridded to 4 m.

c. Density

Float CTD measurements are taken every 15–25 s, i.e., 2.25–3.75 m vertical resolution, and gridded to 4 m. Absolute Salinity S_A, Conservative Temperature Θ, and potential density σ are computed using the Gibbs SeaWater Oceanographic Toolbox of TEOS-10 (McDougall and Barker 2011). Local stratification is calculated using Thorpe-sorted potential density σ_0 referenced to 0 dbar, while unsorted σ_0 is used only for computing reduced shear (sections 5 and 7c) to account for density overturns. Background potential density σ_0^{BG} and stratification N_{BG}^2 profiles are computed using all available sorted float profiles (appendix A).

d. Turbulence

FP07 microthermistors mounted on the float caps sample microscale temperature fluctuations at 125 Hz. Temperature frequency spectra $\Phi_T(\omega)$ are calculated in ~5-s intervals, corresponding to ~0.75-m depth bins. Frequency spectra are converted into vertical wavenumber spectra for temperature gradient $\Phi_{\partial_z T}(k_z)$ after applying three transfer functions: (i) analog-to-digital conversion, (ii) amplification of the high-frequency component provided by the manufacturer, and (iii) double-pole thermistor-response correction (Lien et al. 2016, and references therein).

The EM-APEX float's slow profiling speed allows resolution of high-wavenumber temperature fluctuations, so thermal-variance dissipation rate χ is computed directly by integrating the temperature-gradient spectrum

$$\chi = 6\kappa_T \int_{k_z^{\min}}^{k_z^{\max}} \Phi_{\partial_z T}(k_z)\, dk_z \tag{6}$$

where $\kappa_T = 1.4 \times 10^{-7}$ m^2 s^{-1} is the molecular thermal diffusivity, and $k_z^{\min} = 2$ cpm and $k_z^{\max} = 150$ cpm are the lowest and highest vertical wavenumbers. The highest wavenumbers are dominated by noise or attenuation. If $k_z^{\max}$ is less than the Batchelor wavenumber $k_B = (2\pi)^{-1}(\nu\kappa_T^2/\varepsilon)^{-1/4}$ cpm, where $\nu = 10^{-6}$ m^2 s^{-1} is the kinematic viscosity and ε TKE dissipation rate as estimated from (8), variance contained in the Kraichnan universal spectrum (Kraichnan 1968) between $k_z^{\max}$ and k_B is appended to the integral in (6). Then the Batchelor wavenumber is recalculated from the updated dissipation rates, compared with the previous estimate of k_B, and the variance in the Kraichnan universal spectrum appended if the previous estimate of k_B is still smaller than the updated estimate of k_B. The above procedures are iterated until k_B converges.

Turbulent thermal diffusivity is

$$K_T = \frac{\chi}{2\left(\frac{dT}{dz}\right)^2}, \tag{7}$$

(Osborn and Cox 1972) with background temperature-gradient dT/dz. Assuming that K_T equals turbulent diapycnal diffusivity $K = \Gamma\varepsilon/N^2$ (Osborn 1980), TKE dissipation rate is

$$\varepsilon = \frac{N^2\chi}{2\Gamma\left(\frac{dT}{dz}\right)^2}, \tag{8}$$

where N^2 is the background stratification and $\Gamma = 0.2$ the assumed constant mixing coefficient (Gregg et al. 2018; Monismith et al. 2018). Background values dT/dz and N^2 are computed from local 4-m temperature or potential density profiles. The K_T and ε are not calculated in mixed waters where $dT/dz < 0.002°\mathrm{C\ m^{-1}}$ or $N^2 < 4f^2$.

Measured microscale temperature could be affected by vibration and rotation of the instrument because float buoyancy is adjusted discontinuously and the float is not symmetric. In this study, deviations of observed temperature-gradient spectrum from the Kraichnan (1968) universal spectrum are quantified, and only reasonable data are used (appendix B). Float-inferred profiles of ε were consistent with concurrent VMP measurements (Nagai et al. 2019).

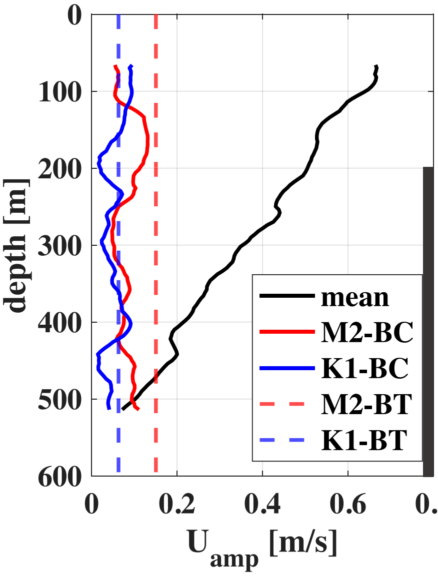

FIG. 2. Profiles of time-mean (black), semidiurnal (M_2; red), and inertial/diurnal (K_1; blue) horizontal speeds $U = \sqrt{u^2 + v^2}$ from harmonic analyses of the upstream ADCP mooring. Curves and dashed lines are baroclinic (BC) and barotropic (BT) tidal components, respectively. The black vertical bar on the right axis indicates the approximate height of Hirase.

3. Dynamic regime of the flow–topography interaction

Qualitative properties of flow–topography interactions can be described using nondimensional parameters, i.e., lee-wave topographic Froude number $\mathrm{Fr}_t = m_{\mathrm{lee}}h_0 \approx N_0h_0/U$, Rossby number $\mathrm{Ro} = U/(fL_0)$, tidal excursion $\mathrm{Ex} = U/(\omega_t L_0)$, and internal-tide steepness $\gamma = m_{\mathrm{tide}}h_0$ (Garrett and Kunze 2007; Legg 2021), where m_{lee} and m_{tide} are lee-wave and internal tide vertical wavenumbers, h_0 and L_0 are vertical and horizontal scales of topography, U is the background mean or tidal current speed, N_0 is background buoyancy frequency, f is Coriolis frequency, and ω_{tide} is tidal frequency.

Fitting the ETOPO1 bathymetry of Hirase to a flat-top Gaussian

$$h(x, y) = h_0 \exp\left\{-\left[\frac{(x - x_0)^2}{L_x^2} + \frac{(y - y_0)^2}{L_y^2}\right]^{p_0}\right\} \tag{9}$$

yields $h_0 = 440$ m and $L_0 = (L_x^2 + L_y^2)^{1/2} = 9.5$ km as its principal vertical and horizontal scales, with flatness $p_0 = 1.8$.

Harmonic analysis of the moored ADCP velocity (u, v) profile time series in terms of a time-mean, inertial/diurnal (K_1), and semidiurnal (M_2) fluctuations was conducted at each depth (e.g., Codiga 2011) (Fig. 2). The upstream current is dominated by the Kuroshio, which decreases linearly with depth. At the 200-m depth of the seamount summit, $U_0 \approx 0.5\ \mathrm{m\ s^{-1}}$ (black curve in Fig. 2). The semidiurnal tidal current $U_t \approx 0.2\ \mathrm{m\ s^{-1}}$ is quasi-barotropic so becomes a potentially significant contributor below 400-m depth (red dashed line in Fig. 2).

Background stratification profiles are similar along the eastern and western trajectories (Fig. 3) with a 100-m thick late-autumn surface mixed layer, a pycnocline with $N_{\mathrm{BG}}^2 \sim 10^{-4}\ \mathrm{s^{-2}}$ between 100- and 250-m depth, and weaker stratification $2–3 \times 10^{-5}\ \mathrm{s^{-2}}$ below 400 m. The near-summit background buoyancy frequency is $N_0 \approx 10^{-2}\ \mathrm{s^{-1}}$.

Based on the bathymetry of Hirase and harmonic analysis of the upstream mooring which reveals that the strongest flows impinging on the seamount are the Kuroshio, it is expected that, to first order, the energetically dominant flow–topography interaction is between the Kuroshio and 10-km-wide bank. This interaction could be complicated by both finer-scale $\mathcal{O}(1)$ km broadband topographic features not resolved by ETOPO1 and oscillatory tidal currents. Using the topographic and background parameters derived above, nondimensional parameters are quantified as

$$\mathrm{Fr}_t = \frac{N_0h_0}{U} \sim 10, \quad \mathrm{Ro} = \frac{U_0}{fL_0} \sim 1, \quad \mathrm{Ex} = \frac{U_t}{\omega_t L_0} \sim 0.2,$$

$$\gamma = \frac{h_0}{L_0}\sqrt{\frac{N_0^2 - \omega_t^2}{\omega_t^2 - f^2}} \sim 4, \tag{10}$$

with high topographic Froude number, steepness and Rossby number, and small excursion parameter. The dynamical implications of these parameter regimes are discussed in more detail below.

a. *Kuroshio–topography interactions*

At Hirase Seamount, topographic Froude number $\mathrm{Fr}_t \gg 1$ so the Kuroshio is energetically unable to move fluid parcels over the full height of topography, resulting in upstream flow-splitting for depths a vertical scale $h_e = U_0/N_0 = 50$ m below the summit (e.g., Baines 1995). Conventional linear lee-wave generation is confined to the summit crown (Nikurashin et al. 2014; Perfect et al. 2020b).

Up- and downgoing slope lee waves may be generated by topographic roughness on the flanks as flow goes around the seamount (Thorpe 1992), although this can be confounded by (i) an arrested Ekman layer shutting off bottom flow on the western flank, and (ii) formation of a thick well-mixed bottom boundary layer on the eastern flank (Trowbridge and Lentz 1991; MacCready and Rhines 1993). Lee waves will be excited by topographic features with horizontal wavenumbers $f/U_0 < k < N/U_0$ (0.1–20-km horizontal wavelengths for $U_0 = 0.5\ \mathrm{m\ s^{-1}}$ summit flow). The Rossby number $\mathrm{Ro} \sim 1$, which is analogous to the

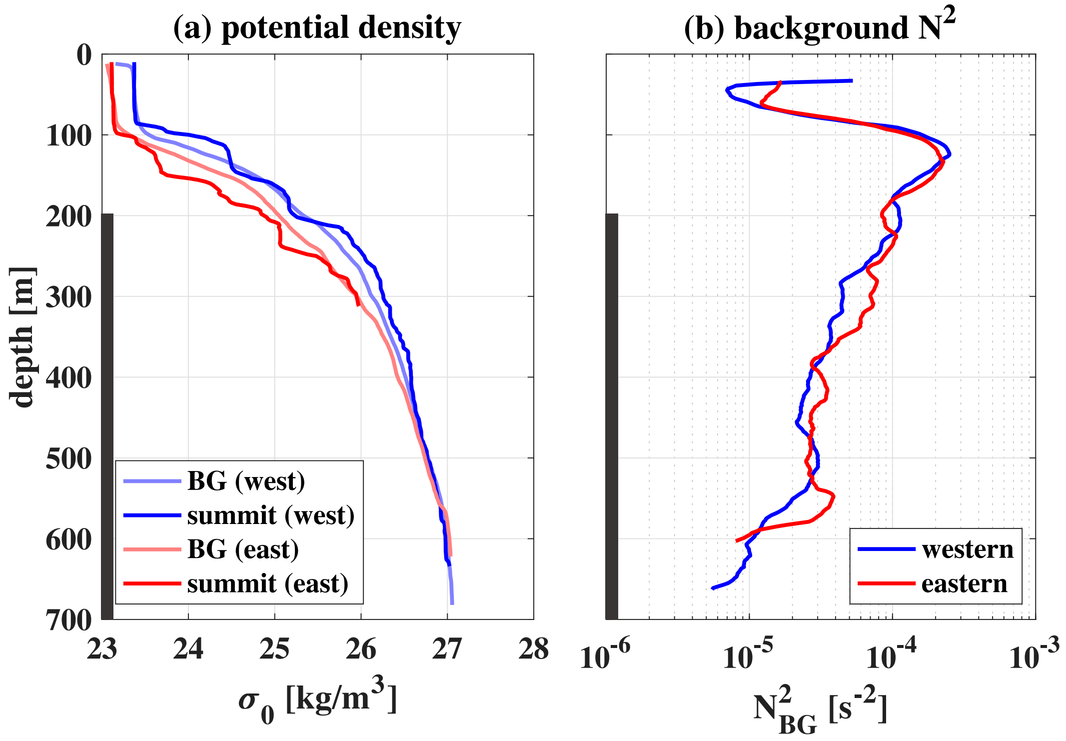

FIG. 3. (a) Example potential density σ_0 (referenced to 0 dbar) profiles near Hirase Seamount summit in the western (darker blue) and eastern (darker red) float trajectories along with background (BG) profiles (lighter colors). (b) Background stratification N^2_{BG} profiles from western (blue) and eastern (red) trajectories. Black vertical bars on the left axes indicate the approximate vertical extent of Hirase.

normalized lee-wave frequency $|kU|/f \sim 1$, suggests generation primarily of near-inertial lee waves.

Flow-splitting around a seamount produces vortex-shedding in the downstream wake (e.g., Baines 1995). Characteristics of the wake depend on topographic Froude number Fr_t and Rossby number Ro measures of the strengths of stratification and rotation, respectively (Perfect et al. 2018, 2020a; Srinivasan et al. 2019, 2021). Nonlinear and highly layered wake structures are expected in the lee of Hirase Seamount for Ro ~ 1 (Srinivasan et al. 2021). Vortices are also expected to be shed from unstable frictional boundary layers on the seamount flanks (D'Asaro 1988; Molemaker et al. 2015).

b. Tide–topography interactions

The tidal-excursion parameter Ex indicates the strength of advection or nonlinearity of tide–topography interactions (e.g., Garrett and Kunze 2007). At Hirase, Ex ≪ 1 suggests internal tide generation will be at the fundamental frequency rather than higher harmonics or quasi-steady lee waves (Bell 1975a; Mohri et al. 2010).

Steepness γ represents the ratio of bottom topographic slope to internal-tide characteristic slope (e.g., Garrett and Kunze 2007). For the semidiurnal frequency, $\gamma > 1$, so internal tides can radiate upward or downward from the summit and flanks, and beams with convective and shear instability can be excited at slope transitions (Balmforth et al. 2002; St. Laurent et al. 2003; Althaus et al. 2003; Nash et al. 2006).

The superposition of steady and oscillatory flow forcing may modulate Kuroshio–topography interactions, but this is not yet well understood. Large-eddy simulations (Puthan et al. 2021) and field observations (Chang et al. 2019; MacKinnon et al. 2019) suggest that the shedding period of wake vortices can become synchronized to subharmonics of the tidal period, and that wake velocity structures vary on the tidal cycle. However, the parameter space corresponding to Hirase conditions has not been fully explored until recently. Three-dimensional numerical simulations of flow–topography interactions at Hirase Seamount suggest that deep-reaching tidal currents can play an essential role in the deeper-layer fluctuations via (i) tidal vortex-shedding and (ii) tidal modulation of the deep current (Inoue et al. 2024).

4. Characteristics of velocity and density fields

EM-APEX float profile time series of velocity reveal that the Kuroshio is blocked or diverted by the seamount in both western and eastern trajectories with Kuroshio flow speeds ~1 m s^{-1} confined above 200-m depth downstream (Figs. 4a–c). At greater depths, along- and across-stream velocities are layered downstream of the seamount, which seems to extend along with isopycnals (Figs. 4a,b,d–f). These flow characteristics are consistent with nonlinear wake structures expected for Hirase's topographic

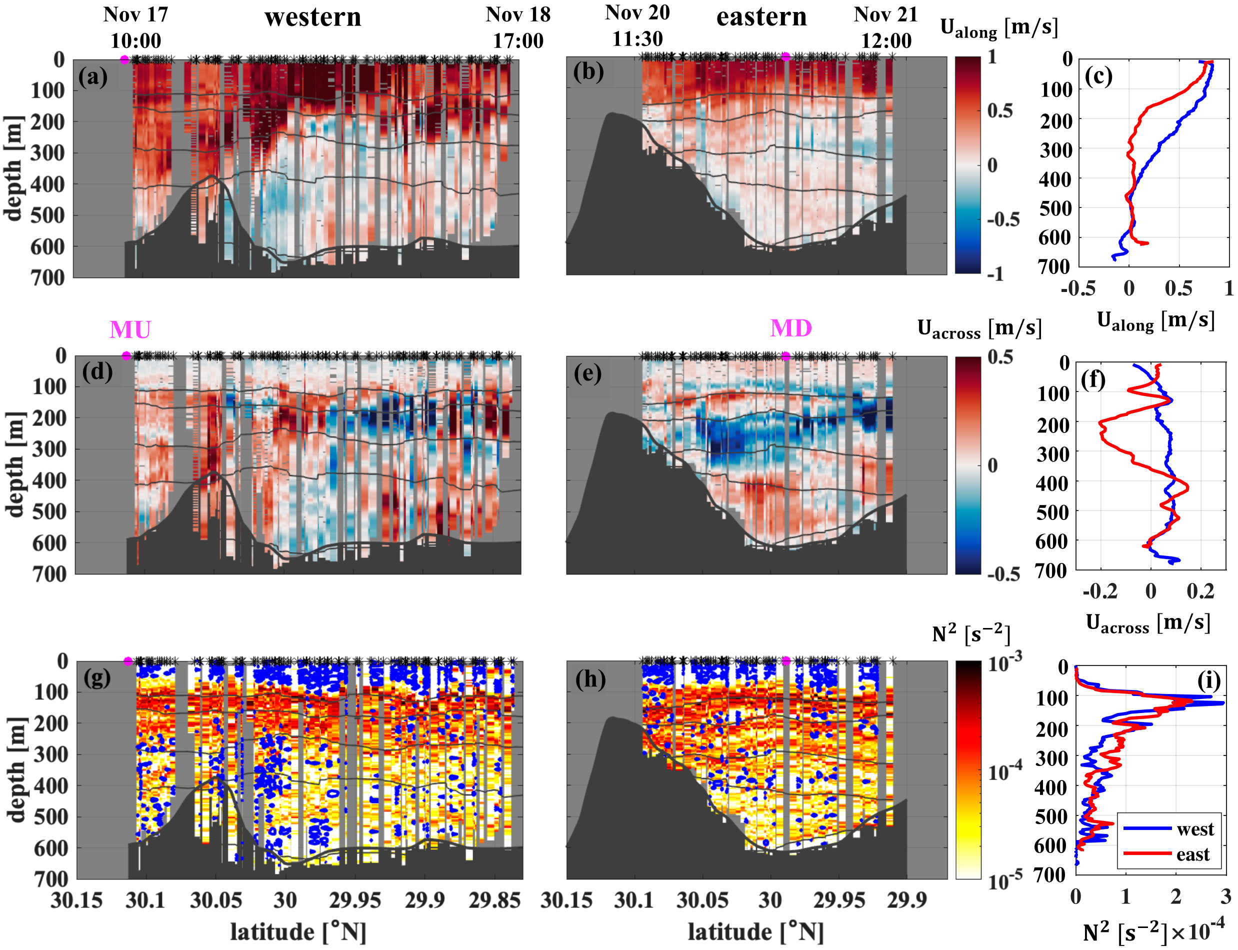

FIG. 4. Profile time series/meridional sections of (a),(b) along-stream velocity, (d),(e) across-stream velocity, and (g),(h) local stratification along (left) western and (center) eastern EM-APEX float trajectories. The along-stream direction is defined for each profile as the average direction of the absolute current velocity in the upper 100 m, representing the Kuroshio. In (g) and (h), 4-m density overturns are blue. Charcoal shading and thick black lines follow the bathymetry at the center of each trajectory from ETOPO1; these do not always agree with the maximum depth of float measurements. Thin black contours show smoothed isopycnals. Black asterisks along the upper axes mark profiles and observation times are indicated above the upper axes of (a) and (b). Magenta labels are upstream (MU) and downstream (MD) mooring locations in (d) and (e), respectively. (right) Ensemble-average vertical profiles for (c) along-stream velocity, (f) across-stream velocity, and (i) local stratification along western (blue) and eastern trajectories (red).

Froude number $\mathrm{Fr}_t > 1$ and Rossby number $\mathrm{Ro} > 1$ (Srinivasan et al. 2021).

Frequency spectra for velocity and shear calculated from ADCP moorings are an order of magnitude higher than the canonical Garrett and Munk (1979) model spectrum (Fig. 5). At both up- and downstream mooring sites, frequency spectra of WKB-normalized horizontal velocity exhibit peaks at inertial/diurnal and semidiurnal frequencies (Figs. 5a,b). Inertial/diurnal signals are stronger downstream than upstream at 100–300-m depth in the pycnocline (Fig. 5a). Semidiurnal signals are stronger upstream than downstream at 300–500-m depth in the deeper layer (Fig. 5b).

Frequency spectra of shear are whiter and smoother than velocity spectra (Figs. 5c,d). In the pycnocline, the shear spectrum is higher downstream than upstream for frequencies ranging from subinertial to supertidal (Fig. 5c). In the deep layer where the Kuroshio is weak, up- and downstream shear spectra are almost identical at all frequencies (Fig. 5d).

Unstable stratification $N^2 < 0$ (>4-m density overturns) is captured by floats (Figs. 4g,h), particularly in the immediate lee of Hirase in the western trajectory. Potential density profiles near the seamount summit have pronounced $\mathcal{O}(10)$ m vertical scale steppiness in the pycnocline (Fig. 3a), which might be due to internal-wave straining or shed bottom boundary layers from the seamount's flanks. The expected change in stratification due to vertical mixing is $\Delta N^2 \sim \int \partial^2(\Gamma\varepsilon)/\partial z^2 dt \sim (\Gamma\varepsilon/\delta z^2)\delta t$ where $\Gamma = 0.2$ is the mixing coefficient, and δz and δt are the turbulent-layer vertical and time scales, respectively (Essink et al. 2022). Plugging in measured numbers, i.e., $\varepsilon \sim 10^{-6}$ W kg^{-1} (section 5), $\delta z \sim 10$ m and $\delta t \sim L_0/U_0 \sim 2 \times 10^4$ s (section 3), and

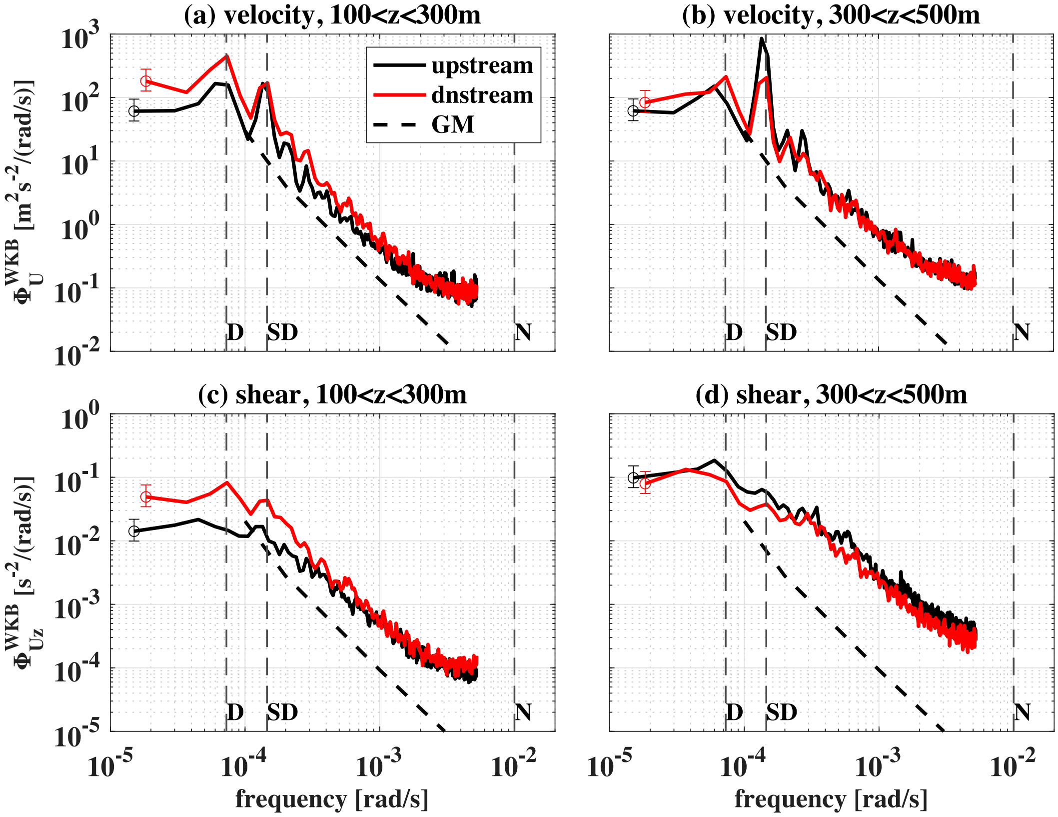

FIG. 5. Frequency spectra of WKB-normalized (a),(b) horizontal velocity and (c),(d) vertical shear obtained from upstream (black curves) and downstream (red curves) moorings along with Garrett–Munk model spectra (dashed curves). Spectra are averaged over (left) the pycnocline (100–300 m) and (right) the deeper layer (300–500 m). Dashed vertical lines indicate inertial/diurnal (D), semidiurnal (SD) and buoyancy (N) frequencies. Error bars indicate the 95% confidence intervals of spectra (Thomson and Emery 2014).

$\Delta N^2 \sim 4 \times 10^{-5}$ s^{-2}. This is the same order as the measured weakening, so diapycnal turbulent mixing might account for the steppiness.

5. Layers of enhanced turbulent mixing extended downstream

Around Hirase, background TKE dissipation rates $\varepsilon \sim 10^{-8}$ W kg^{-1} and diapycnal diffusivities $K \sim 10^{-4}$ m^2 s^{-1} are an order of magnitude higher than in typical open-ocean pycnoclines (Fig. 6). Turbulence is particularly enhanced with $\varepsilon \sim 10^{-6}$ W kg^{-1} and $K \sim 10^{-2}$ m^2 s^{-1} over the seamount flanks and at ~150–250-m depths extending at least 20 km downstream. In the eastern deployment, a strong turbulence layer with $\varepsilon \sim 10^{-7}$ W kg^{-1} and $K \sim 10^{-2}$ m^2 s^{-1} is also evident at ~350–450-m depth, extending about 10 km downstream (Figs. 6d,f).

Previous observations and numerical simulations suggest that Kuroshio–Hirase interactions shed asymmetric vortices in the downstream wake (Nagai et al. 2021; Inoue et al. 2024). These will have positive vorticity on the western flank so more likely to be stable, and negative vorticity on the eastern flank so more unstable, consistent with the observed turbulence that seems more enhanced in the eastern trajectory than western in the upper 200 m.

Enhanced TKE dissipation rates are associated with 4-m reduced shear squared $|\mathbf{v}_z|^2 - 4N^2 > 0$, suggestive of shear instability (Fig. 7). The 4-m squared gradient Froude number $\mathrm{Fr}^2 = |\mathbf{v}_z|^2/N^2$ is elevated compared to shear variance normalized by background stratification, $|\mathbf{v}_z|^2/N_{\mathrm{BG}}^2$ (Fig. 8), suggesting that shear instability arises from reduced stratification as well as enhanced shear. Near the seamount in the western section, shear variance alone is high enough to induce instability (Fig. 8d).

Mooring time series of normalized shear variance $|\mathbf{v}_z|^2/N_{\mathrm{BG}}^2$ provide a proxy for the temporal variability of turbulence (Fig. 9), though normalized shear variance may underestimate squared gradient Froude number Fr^2. Normalized shear variance is typically ~1 but enhanced in intermittent patches (Fig. 9). The upstream mooring shows patches of high shear at 400–500-m depth (Fig. 9a). The downstream mooring shows downward phase propagation in inertial/diurnal shear at 100–300-m depth (Fig. 9b), reminiscent of simulations in which inertial oscillations and lee waves are excited by steady flow interacting with topography (Nikurashin and Ferrari 2010; Zemskova and Grisouard 2021). Time-averaged

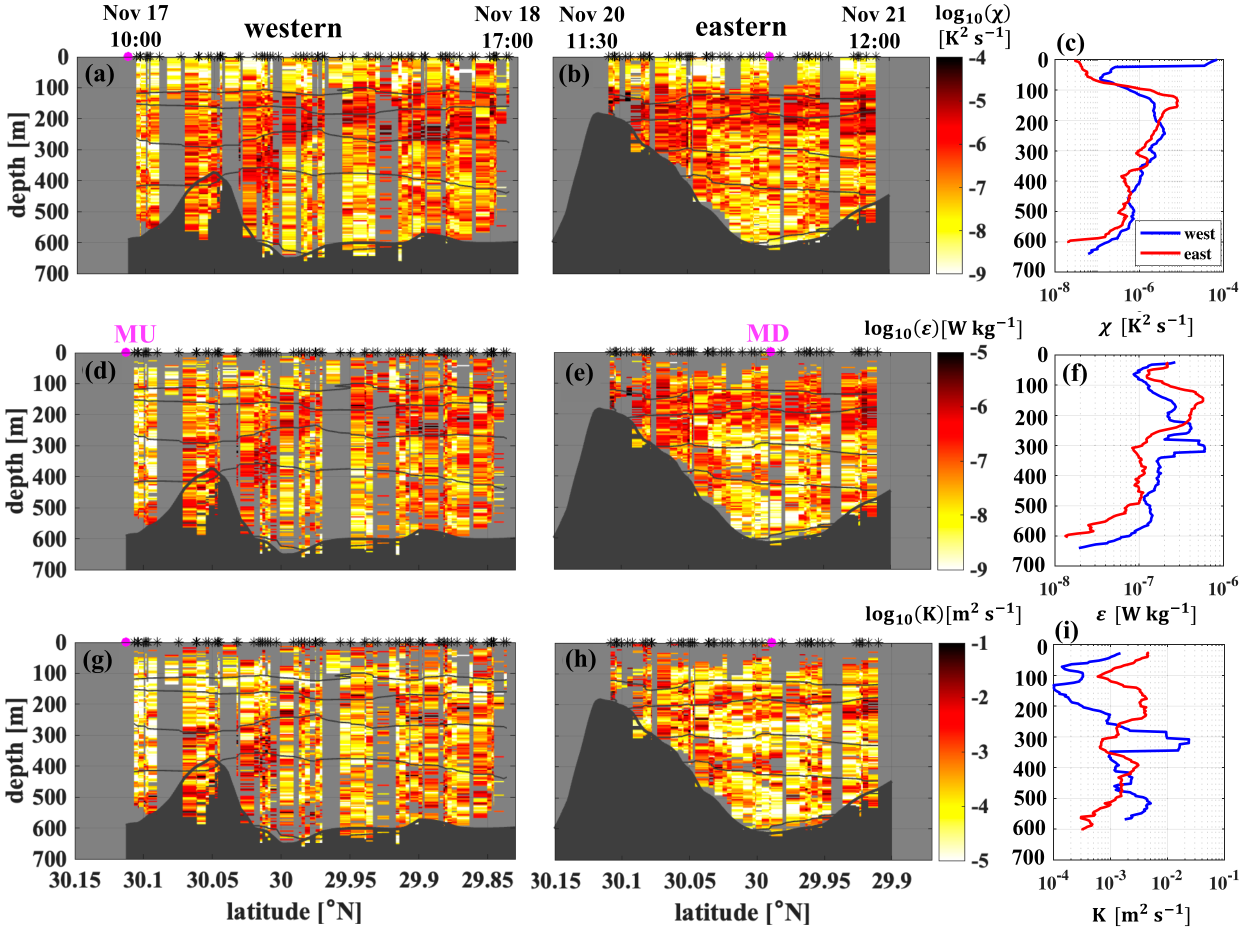

FIG. 6. Depth–latitude sections (time series) of (a),(b) thermal-variance dissipation rate χ, (d),(e) turbulent kinetic energy dissipation rate ε, and (g),(h) diapycnal diffusivity K along the (left) western and (center) eastern EM-APEX float trajectories. Charcoal shading and thick black lines follow the bathymetry at the center of each trajectory from ETOPO1; these do not always agree with the maximum depth of float measurements. Thin black contours show smoothed isopycnals. Black asterisks along the upper axes mark the profiles and observation times are indicated above the upper axes of (a) and (b). Magenta labels are upstream (MU) and downstream (MD) mooring locations in (d) and (e), respectively. (right) Ensemble-average vertical profiles for (c) χ, (f) ε, and (i) K along western (blue) and eastern (red) trajectories are vertically smoothed over 40 m.

mooring shear variances are consistent with average EM-APEX shear variances (Figs. 9c,d) though average EM-APEX shears are higher than mooring shears at 400-m depth upstream and 200-m depth downstream, possibly due to the intermittent high-shear patches at these depths evident in the mooring.

The energetic turbulent layer at 150–250-m depth (Fig. 6) is consistent with previous observations of a turbulent layer extending 100 km downstream of Hirase (Nagai et al. 2017, 2019, 2021). Since isotropic turbulence is thought to persist for $\sim\mathcal{O}(N^{-1})$ after generation (Ozmidov 1965), isotropic turbulence generated over the seamount by lee-wave hydraulics (Hasegawa et al. 2021) or frictional bottom boundary layers (D'Asaro 1988) should only be advected $U/N < \mathcal{O}(100)$ m by the Kuroshio. This suggests that the persistent turbulence extending 100 km downstream of the seamount must be maintained by continuous replenishment.

Such continuous turbulence production could arise from local nonlinear instabilities of a marginally stable wake. Nagai et al. (2021) reported the turbulent layers were associated with negative potential vorticity, suggesting that inertial-symmetric or secondary Kelvin–Helmholtz instabilities play a role in far-field turbulent mixing. Unfortunately, our EM float data do not allow computation of PV. Alternatively, Kunze (2019) argued that anisotropic stratified turbulence generated at the seamount could continuously feed energy into isotropic turbulence for duration of $\sim\mathcal{O}[(1-10)f^{-1}]$ equivalent to a 10–100-km turbulent wake.

The turbulence layer in the pycnocline might also be caused by breaking lee waves advected downstream by the Kuroshio (Zheng and Nikurashin 2019). Because of the high topographic Froude number, lee-wave generation is confined to the seamount's summit. These waves will be trapped within the Kuroshio by the $|U| = |f/k|$ isotach (Kunze and Lien 2019).

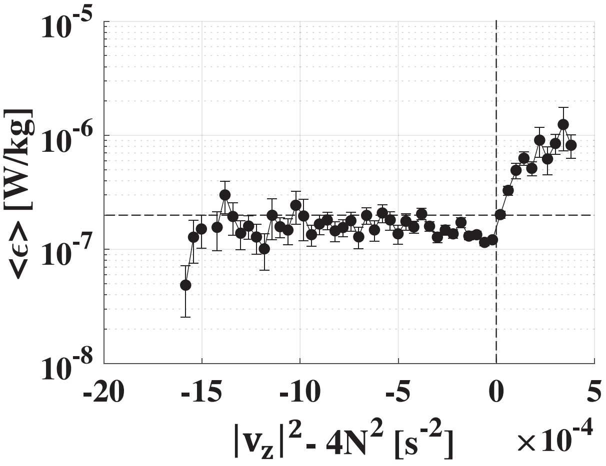

FIG. 7. Relationship between turbulent kinetic energy dissipation rate ε and 4-m reduced shear $|\mathbf{v}_z|^2 - 4N^2$, where N^2 is local stratification and $|\mathbf{v}_z|^2$ vertical shear squared. Dissipation rates are binned by values of reduced shear with mean (dots) and standard error (vertical bars) of ε calculated for each bin. For clarity, bins with less than 10 data points are excluded. The 2×10^{-7} W kg^{-1} level (dashed horizontal line) below $|\mathbf{v}_z|^2 - 4N^2 = 0$ (dashed vertical line) represents the expected noise level for 4-m reduced shear at $N \sim 10^{-2}$ s^{-1}.

Ray-tracing calculations (Lighthill 1978) are performed for summit-generated lee waves (appendix C) using observed horizontal velocity $U(z)$ and buoyancy frequency $N(z)$ profiles (Fig. 10b). Upward-propagating lee waves reflect either from the surface (Fig. 10a) or vertical turning points z_N where $|kU(z_N)| = N(z_N)$ at the base of the mixed layer. Reflected or bottom-generated downward-propagating lee waves encounter vertical critical layers at depths z_f such that $|kU(z_f)| = f$ where trapping, stalling, and amplification are expected to lead to breaking and turbulence production (Kunze 1985; Kunze et al. 1995). The predicted 200–300-m critical-layer depths (Fig. 10a) bracket the observed layer of high turbulent dissipation (Fig. 6). Lee waves carried downstream in Fig. 10a have initial intrinsic frequencies $|kU| < 2.5f$ and final vertical wavenumbers $|m| = 0.02$ cpm. They are carried 20 km downstream in less than 2 days. These near-inertial lee waves could be the cause of high-vertical-wavenumber shear along isopycnals in the downstream of Hirase reported by Nagai et al. (2019, 2021). Higher-frequency (initial $|kU| > 2.5f$) lee waves are confined above the seamount, reflecting from the surface or base of the mixed layer to return to the summit where they may break or impact lee-wave generation (Baker and Mashayek 2021). Since none of the lee waves reach 400-m depth, the elevated turbulence in this layer (Fig. 6) must have another cause such as instabilities in the wake or anisotropic stratified turbulence.

6. Vertical wavenumber spectra

EM-APEX float vertical wavenumber spectra for normalized shear $\mathbf{v}_z/\overline{N}$, where $\overline{N}$ is depth-averaged N_{BG}, vertical strain $\eta_z = (N^2 - N_{\mathrm{BG}}^2)/N_{\mathrm{BG}}^2$, and vertical divergence w_z are computed in half-overlapping 200-m segments below the mixed layer then binned by depth-averaged TKE dissipation rate $\overline{\varepsilon}$ (Fig. 11). Composite EM float shear spectra are corrected for 7.5-m smoothing (Polzin et al. 2002) (see section 2a). Vertical strain and divergence spectra are corrected for first differencing (Polzin et al. 2002; Whalen et al. 2015). Ozmidov wavenumbers $m_O = (2\pi)^{-1}\sqrt{N^3/\varepsilon}$ (cpm) are only in the resolved vertical wavenumber range for $\varepsilon \sim 7.7 \times 10^{-7}$ W kg^{-1} (red vertical lines in Fig. 11), so the outer scales of isotropic turbulence are only captured for the strongest turbulence.

Shear and strain spectra are an order of magnitude above the canonical GM spectral level (Garrett and Munk 1975; Cairns and Williams 1976; Gregg and Kunze 1991) (Figs. 11a,b). They have spectral slopes of -1 for wavenumbers $m > 0.01$ cpm, and their spectral levels show no dependence on turbulence intensity, indicating saturation for which vertical shears $|\mathbf{v}_z| \sim N$ (Dewan 1979; Gargett et al. 1981). Spectral roll-offs are at slightly higher wavenumber for strain ($m_c \approx 0.02$ cpm) than shear ($m_c \approx 0.01$ cpm). Thus, flows are marginally unstable (Smyth 2020) on wavelengths of $\mathcal{O}(100)$ m, comparable to the water depth which places them in the wave–turbulence transition (D'Asaro and Lien 2000b) of anisotropic stratified turbulence (Kunze 2019).

Vertical divergence spectra are one to two orders of magnitude higher than the canonical GM level, with $|w_z| \sim N$ for the strongest turbulence (Fig. 11c). In contrast to the shear and strain spectra, w_z spectral levels increase with turbulent intensity and the spectra do not roll off for strongest turbulence. The latter could be because (i) vertical divergence is dominated by near-buoyancy frequency waves (Desaubies 1975) in contrast to shear and strain spectra dominated by near-inertial waves, or (ii) a turbulence contribution. Consistent with (i), Sherman and Pinkel (1991) found that the roll-off wavenumber increased with increasing frequency.

The finescale ratio of horizontal kinetic to available potential energy HKE/APE is near the GM value of 3 at low vertical wavenumbers, decreasing to 1 at higher wavenumbers, regardless of dissipation rate (Fig. 12a). The finescale ratio of horizontal to vertical kinetic energy HKE/VKE is close to the GM value of ~80 at low wavenumbers and lower turbulent intensities but drops precipitously at high vertical wavenumbers for the strongest turbulence, where flows become almost isotropic (Fig. 12b). The decreases at higher wavenumber could be due to (i) superinertial internal waves (Desaubies 1975) or (ii) turbulence.

Measurements of vertical velocity w in the ocean are rare. Thurnherr et al. (2015) found that vertical wavenumber spectra of vertical divergence at several open ocean sites were consistent with the GM internal-wave spectral model

$$\Phi_{\mathrm{GM}}[w_z](m) = 0.5E_0\sqrt{\frac{\varepsilon}{\varepsilon_{\mathrm{GM}}}}bNfj^*\frac{(2\pi m)^2}{(m^* + m)^2}, \qquad (11)$$

where $E_0 = 6.5 \times 10^{-5}$, $\varepsilon_{\mathrm{GM}} = 7.0 \times 10^{-10}$ W kg^{-1}, $b = 1300$ m, $j^* = 3$, and $m^* = j^*/(2b)$.

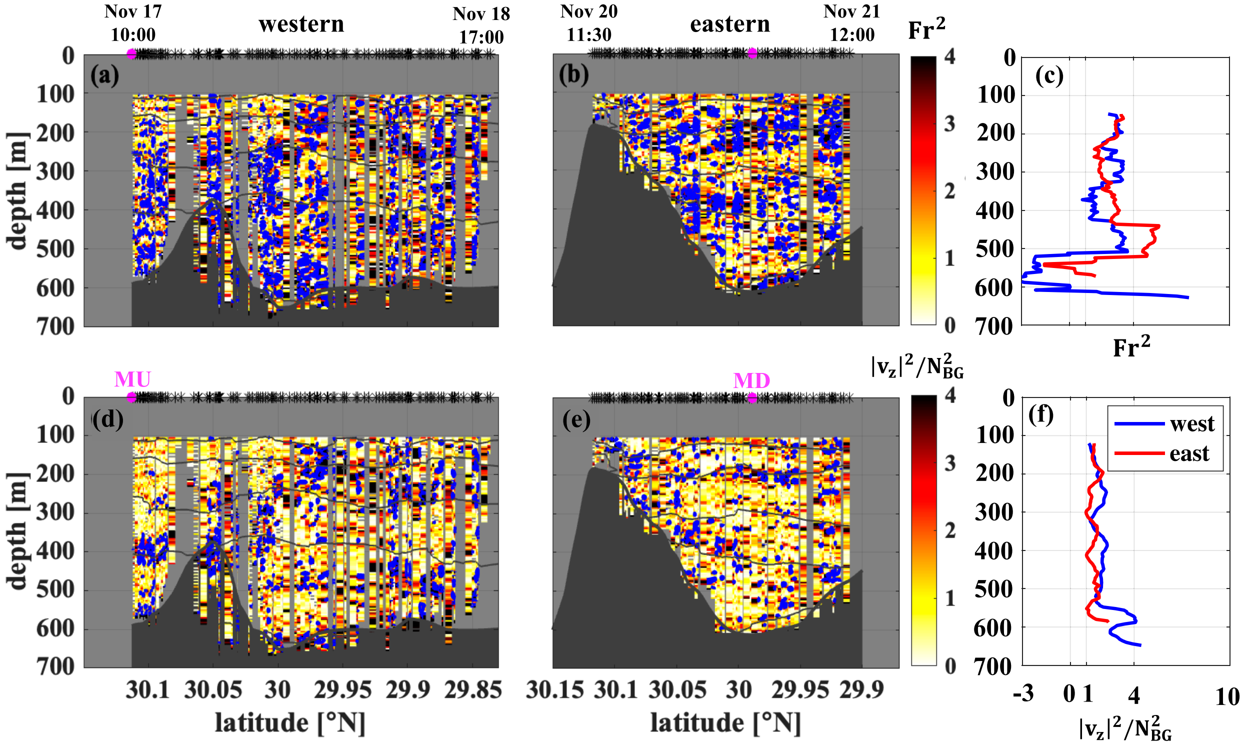

FIG. 8. Vertical cross sections of (a),(b) 4-m squared gradient Froude number $Fr^2 = |\mathbf{v}_z|^2/N^2$ and (d),(e) shear variance normalized by background stratification $|\mathbf{v}_z|^2/N^2_{BG}$ along (left) western and (center) eastern EM-APEX float trajectories; blue contours mark where Fr^2 [in (a) and (b)] or $|\mathbf{v}_z|^2/N^2_{BG}$ [in (d) and (e)] exceed the instability criterion of 4. Surface mixed layer data are excluded for clarity. Charcoal shading and thick black lines follow the bathymetry at the center of each trajectory obtained from ETOPO1; this does not always agree with the maximum depth of float measurements. Thin black contours show smoothed isopycnals. Black asterisks along the upper axes mark profiles and observation times are indicated above the upper axes of (a) and (b). Magenta labels are upstream (MU) and downstream (MD) mooring locations in (d) and (e), respectively. (right) Ensemble-average vertical profiles along the western (blue) and eastern (red) trajectories are vertically smoothed (c) over 100 m for Fr^2 and (f) over 40 m for $|\mathbf{v}_z|^2/N^2_{BG}$.

Kunze (2019) argued that isotropic turbulence (ISO) dimensional scaling (Kolmogorov 1941; Batchelor 1953; Ozmidov 1965; Tennekes and Lumley 1972; Thorpe 2005) applies above the Ozmidov wavenumber, $m > m_O$, while anisotropic stratified turbulence (ANISO) scaling should be applied between the roll-off and Ozmidov wavenumbers, $m_c < m < m_O$. Here, ISO spectra are modeled as

$$\Phi_{ISO}[w_z](m) = 5.5\varepsilon^{2/3}m^{1/3}, \qquad (12)$$

where the coefficient is determined from the Nasmyth universal turbulent shear spectra (Nasmyth 1970; Oakey 1982), and ANISO spectra as

$$\Phi_{ANISO}[w_z](m) \propto \varepsilon^2 m^2 N^{-4} \qquad (13)$$

(Kunze 2019) where the amplitude is set such that Φ_{ANISO} agrees with Φ_{ISO} at $m = m_O$.

At lower vertical wavenumbers (<0.02 cpm), observed vertical divergence spectra are roughly consistent with GM (11) spectral levels and shapes while model ANISO (13) turbulence has much lower spectral levels (Fig. 13). At higher vertical wavenumbers and lower measured $\varepsilon < 1.3 \times 10^{-7}$ W kg^{-1}, observed spectra roll off below GM with levels consistent with ANISO model spectra at the highest vertical wavenumber. At high vertical wavenumbers and the highest measured $\varepsilon \sim 7.7 \times 10^{-7}$ W kg^{-1}, measured spectra are consistent with both GM and the ANISO/ISO turbulence transition which cannot be distinguished. We interpret this figure as signifying that vertical wavenumbers less than a few times 10^{-2} cpm are linear internal waves while turbulence dominates wavenumbers $\mathcal{O}(10^{-1})$ cpm.

To summarize this section, observed vertical wavenumber spectra of shear, strain, and vertical divergence suggest 10–100-m vertical scales correspond to the transition between internal waves and turbulence. Vertical divergence spectral levels are compatible with GM levels at $\sim 10^{-2}$ cpm, even though this scale is in the -1 spectral slope regime for shear and strain. The ANISO turbulence model lies below measured vertical divergence at low wavenumbers but becomes comparable at the highest vertical wavenumbers. Finer vertical resolution measurements are needed for more definitive conclusions.

7. Comparison with turbulent parameterizations

In this section, the validity of three turbulence parameterizations is examined for the energetic turbulence observed in

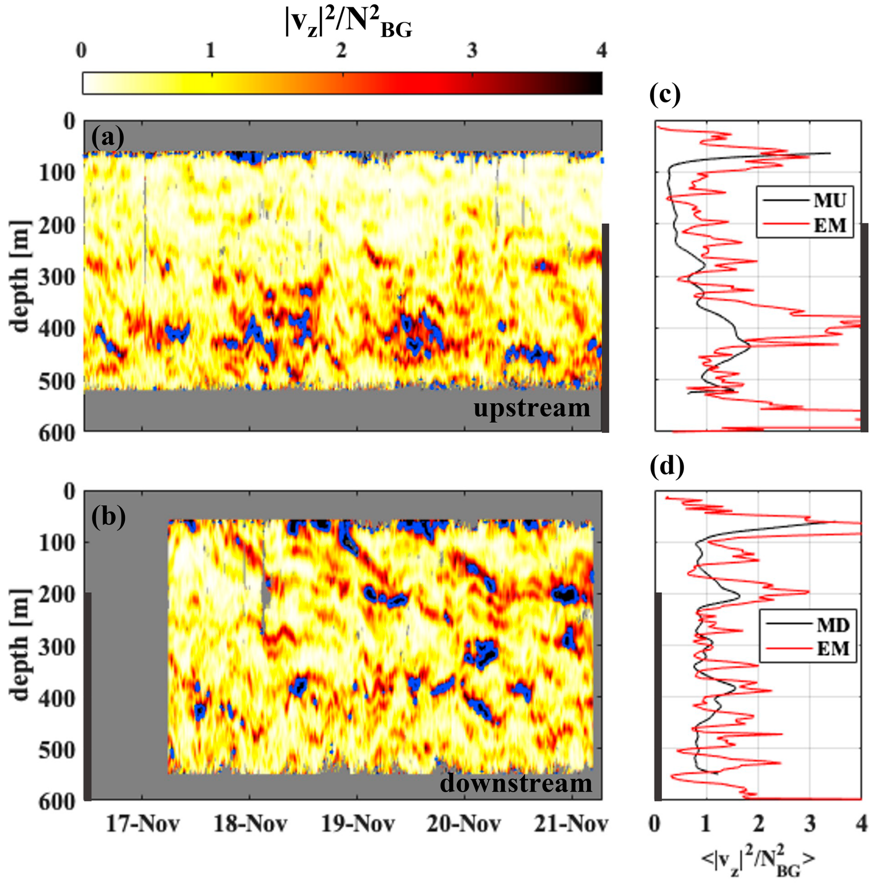

FIG. 9. (left) Time series of buoyancy-normalized shear variance $|\mathbf{v}_z|^2/N_{\mathrm{BG}}^2$ from (a) upstream and (b) downstream moorings. Blue contours indicate $|\mathbf{v}_z|^2/N_{\mathrm{BG}}^2$ exceeding 4. (right) Comparison between mean normalized shear variances from moorings (black) and EM-APEX floats (red) near the (c) upstream (MU) and (d) downstream (MD) moorings. Black vertical bars along the vertical axes indicate the approximate height of Hirase.

Tokara Strait—finescale (Gregg 1989; Polzin et al. 1995), large eddy (Moum 1996; D'Asaro and Lien 2000b), and reduced shear (Kunze et al. 1990).

a. *Finescale parameterization*

In the midlatitude open-ocean interior, turbulence tends to be modest and generated by weakly nonlinear internal wave–wave interactions cascading energy toward smaller scales (McComas and Müller 1981; Henyey et al. 1986). The finescale parameterization (e.g., Gregg 1989; Polzin et al. 1995; Gregg et al. 2003) provides estimates of dissipation rate ε using finescale shear variance $\langle \mathbf{v}_z^2 \rangle$ normalized by the GM values $\langle \mathbf{v}_z^2 \rangle_{\mathrm{GM}}$

$$\varepsilon_{\mathrm{FS}} = \varepsilon_0 \cdot \frac{N^2}{N_0^2}\left(\frac{\langle \mathbf{v}_z^2 \rangle}{\langle \mathbf{v}_z^2 \rangle_{\mathrm{GM}}}\right)^2 \frac{3\sqrt{2}(R_\omega + 1)}{4R_\omega\sqrt{R_\omega - 1}}, \qquad (14)$$

and shear-to-strain variance ratio

$$R_\omega = \frac{\langle \mathbf{v}_z^2 \rangle}{N^2 \langle \eta_z^2 \rangle}, \qquad (15)$$

where $\varepsilon_0 = 6.3 \times 10^{-10}$ W kg^{-1} and $N_0 = 5.2 \times 10^{-3}$ s^{-1}.

Shear and strain variances are usually computed by integrating vertical wavenumber spectra over the wavenumber band below spectral roll-offs for comparison with GM variances (Gregg and Kunze 1991). Since measured spectra in Tokara Strait have roll-offs on length scales comparable to the water depth, vertical profiles of ε cannot be obtained by this method. As a compromise, first-difference shear and strain are calculated from horizontal velocity and density profiles vertically smoothed using a 50-m cutoff low-pass filter. The 50-m shear and strain variances are averaged over a moving 50-m window and substituted into (14) following Gregg (1989). The 50-m first differences resolve wavenumbers less than 0.1 cpm, which are outside the saturated wave band and in the weakly nonlinear wave regime, so the finescale parameterization should be valid (Gargett 1990; Gregg and Kunze 1991; Polzin et al. 2014b).

Finescale $\varepsilon_{\mathrm{FS}}$ and simultaneously obtained microstructure $\varepsilon_{\mathrm{micro}}$ have low correlation coefficient $R = 0.17$ (Fig. 14a), as expected for the finescale parameterization which was never intended to capture individual events (Henyey et al. 1986; Gregg 1989; Polzin et al. 1995; Kunze et al. 2006; Polzin et al.

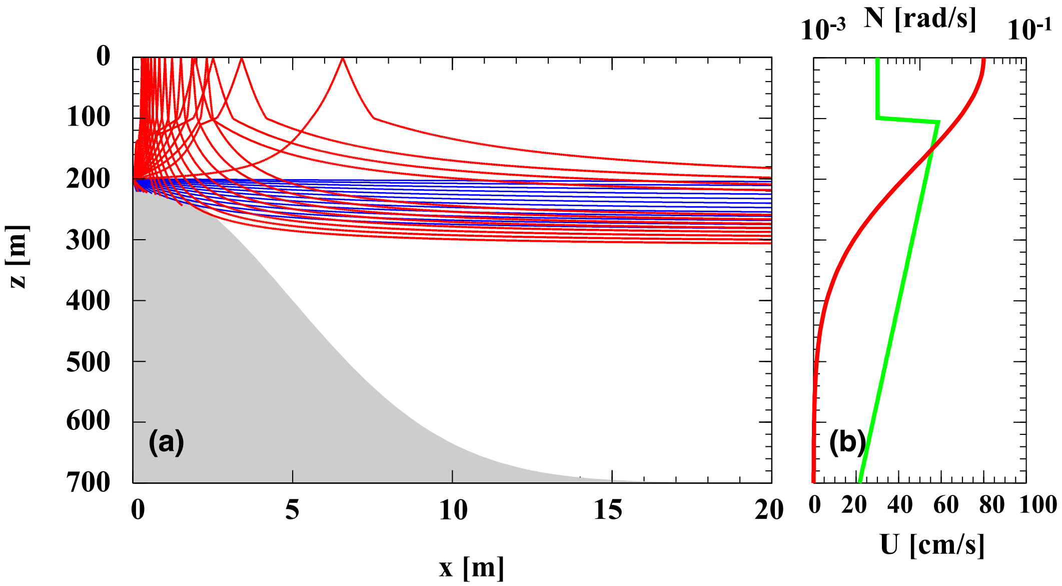

FIG. 10. (a) Lee-wave ray paths originating from Hirase summit. Upward-propagating waves reflect off the surface or base of the mixed layer where $|kU(z_N)| = N(z_N)$ then propagate downward to encounter vertical critical layers as $|kU(z_f)| \to f$ at depths of 200–300 m (red). Downward-propagating lee waves directly encounter critical layers (blue). (b) Polynomial fits to pycnocline buoyancy frequency (green) and along-stream flow (red) profiles used for the ray tracing.

2014b). However, ensemble-average vertical profiles of finescale $\langle \varepsilon_{\rm FS} \rangle$, as appropriate for this bulk parameterization, and microstructure $\langle \varepsilon_{\rm micro} \rangle$ are correlated with $R = 0.62$ (Fig. 15). Finescale estimates $\langle \varepsilon_{\rm FS} \rangle$ are as much as 3 times smaller than microstructure $\langle \varepsilon_{\rm micro} \rangle$. This may be due to contamination by the saturated vertical wavenumber spectra, which will lead to finescale underestimation of ε because the spectral level is normalized by the GM value in (14) (Gargett 1990; Gregg and Kunze 1991).

b. *Large-eddy parameterization*

Oceanic Lagrangian frequency spectra of vertical velocity exhibit a sharp drop at $\hat{\omega} = N$, separating internal waves from turbulence (Cairns and Williams 1976; D'Asaro and Lien 2000a). D'Asaro and Lien (2000b) argued that, as internal-wave energy increases, this spectral level drop at N closes until the internal-wave and turbulent spectra become smoothly connected across $\hat{\omega} = N$. This implies that the relationship between internal-wave energy E and turbulent dissipation rate ε

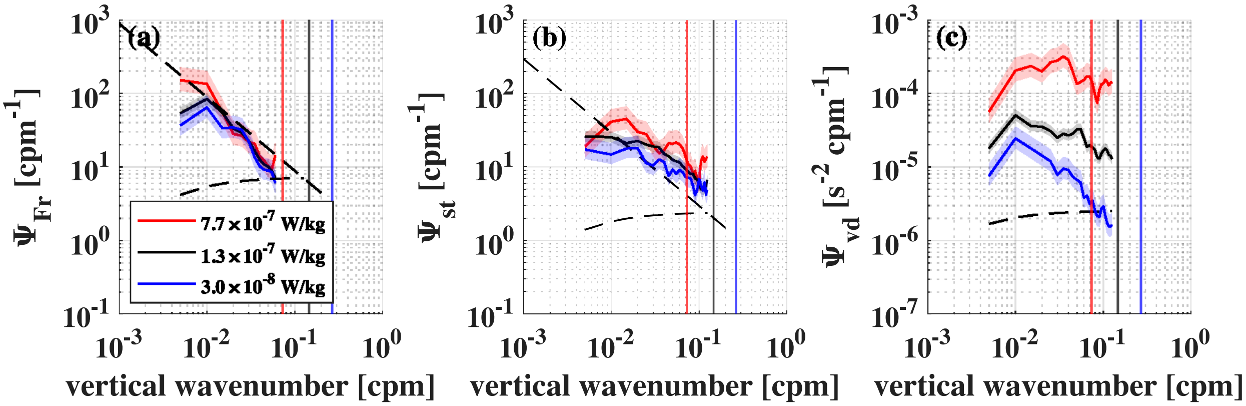

FIG. 11. Composite vertical wavenumber spectra for (a) normalized shear, (b) vertical strain, and (c) vertical divergence from 200-m half-overlapping EM-APEX profile segments below the mixed layer binned by depth-averaged dissipation rate $\overline{\varepsilon}$ [legend in (a)]. Shading denotes the 95% confidence interval (Thomson and Emery 2014). Dashed black lines are canonical-level Garrett–Munk spectra and saturated spectra with -1 spectral slopes. Colored vertical lines indicate the Ozmidov wavenumbers $m_O = (2\pi)^{-1}\sqrt{N^3/\epsilon}$ (cpm) for the different $\overline{\varepsilon}$.

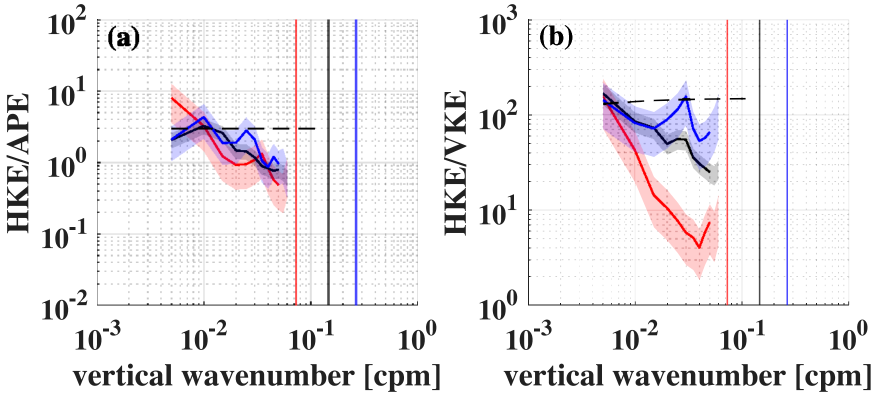

FIG. 12. Ratios of vertical wavenumber spectra of (a) horizontal kinetic energy HKE to available potential energy APE and (b) HKE to vertical kinetic energy VKE from composite spectra in Fig. 11. Colors denote different dissipation rates $\overline{\varepsilon}$ (red: 7.7×10^{-7}, black: 1.3×10^{-7}, and blue: 3.0×10^{-8} W kg^{-1}) as in Fig. 11. Shading denotes 95% confidence (Thomson and Emery 2014). Dashed black lines are the Garrett–Munk $(\mathrm{HKE/APE})_{\mathrm{GM}} = 3$ and $(\mathrm{HKE/APE})_{\mathrm{GM}} = 80$ ratios. Colored vertical lines indicate Ozmidov wavenumbers for the different $\overline{\varepsilon}$.

transitions from that of weakly nonlinear wave–wave interactions with $\varepsilon \propto E^2$ (McComas and Müller 1981; Henyey et al. 1986) to stratified turbulence with $\varepsilon \propto E$ (Mellor and Yamada 1982; Kunze and Lien 2019). In terms of vertical wavenumber spectra, this *wave–turbulence transition* from weak to strong turbulence occurs in the wave band between the roll-off wavenumber m_c and the Ozmidov wavenumber m_O (~0.01–0.1 cpm in Figs. 11a,b).

D'Asaro and Lien (2000b) proposed that (i) finescale parameterization (14) works for weakly nonlinear internal wave–wave interactions while (ii) the large-eddy (or stratified turbulence) parameterization

$$\varepsilon_{\mathrm{LE}} = cN\langle w^2\rangle \tag{16}$$

with coefficient c and vertical velocity variance $\langle w^2\rangle$ for energetic stratified turbulence. Equation (16) has a similar form to the two-equation stratified turbulence model (Mellor and Yamada 1982; Burchard et al. 1998) and is analogous to isotropic turbulence dimensional scaling (Taylor 1935) applied at the Ozmidov scale L_O

$$\langle w^2\rangle \sim \varepsilon N^{-1} = N^2 L_O^2. \tag{17}$$

The large-eddy parameterization has been substantiated by field observations in the midlatitude thermocline (Moum 1996; Evans et al. 2018) and mixed layer (Evans et al. 2018), upper equatorial Pacific (Lien et al. 1996; D'Asaro and Lien 2000b), and Nordic seas overflows (Beaird et al. 2012). Our $\langle w^2\rangle$ measurements include internal-wave and turbulence contributions though turbulent motions may be only partially captured, and internal-wave $\langle w^2\rangle$ variance is dominated by large vertical scales. Following Beaird et al. (2012), a fourth-order high-pass Butterworth filter with cutoff vertical wavelength $\lambda_z = 30$ m is applied to remove the larger-scale internal-wave contribution not associated with turbulence. This cutoff wavelength is a compromise between the measurement's 4-m vertical resolution and the 100-m vertical scales of internal waves. The residual vertical velocity variances are averaged over a 30-m window and substituted into (16). Large-eddy $\varepsilon_{\mathrm{LE}}$ and microstructure $\varepsilon_{\mathrm{micro}}$ have correlation $R = 0.54$ (Fig. 14b).

Coefficient c in (16) depends on the vertical scales of $\langle w^2\rangle$ so is a source of uncertainty. Beaird et al. (2012) derived $c = 0.37$ from a linear least squares fit to microstructure data. We find

$$c = 1.9 \tag{18}$$

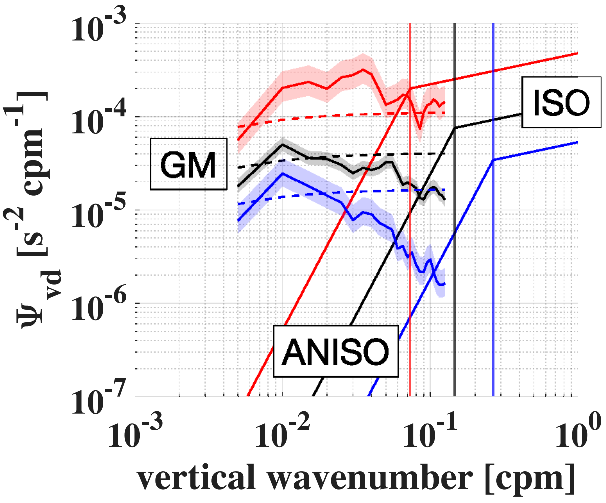

FIG. 13. Comparison of vertical wavenumber spectra for vertical divergence with Garrett–Munk internal-wave (11) (dashed line), isotropic (12) (solid line at high wavenumbers), and anisotropic turbulence (13) (solid line at low wavenumbers) models. Colors denote different dissipation rates $\overline{\varepsilon}$ (red: 7.7×10^{-7}, black: 1.3×10^{-7}, and blue: 3.0×10^{-8} W kg^{-1}) as in Fig. 11. Shading denotes 95% confidence (Thomson and Emery 2014). Colored vertical lines indicate Ozmidov wavenumbers for the different $\overline{\varepsilon}$.

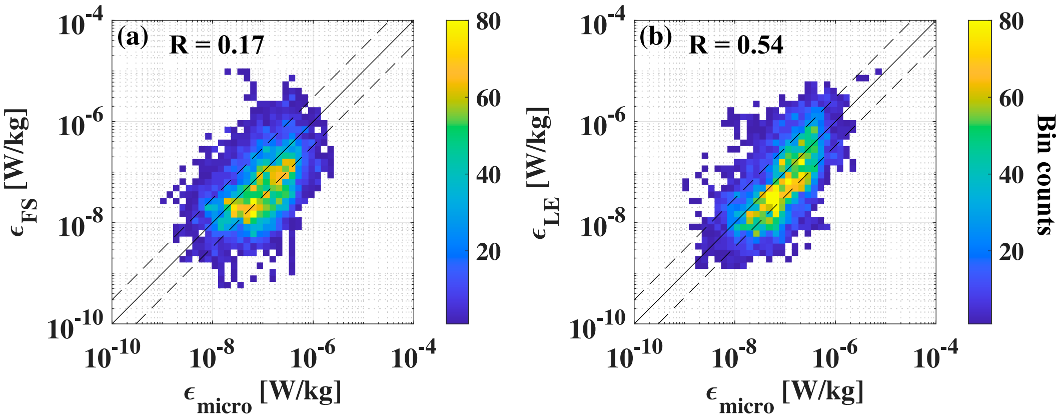

FIG. 14. Scatterplots of turbulent kinetic energy dissipation rates from the (a) finescale parameterization $\varepsilon_{\mathrm{FS}}$ and microstructure-inferred $\varepsilon_{\mathrm{micro}}$ and (b) large-eddy parameterization $\varepsilon_{\mathrm{LE}}$ and $\varepsilon_{\mathrm{micro}}$. Each estimate is smoothed over a 52-m vertical window to compare all estimates consistently. Colors indicate data number in each bin. Solid diagonal lines mark one-to-one correspondence, and dashed lines mark a factor-of-3 agreement. Correlation coefficients R between two estimates are shown in each panel.

best explains our data (Fig. 14b), even though the same cutoff vertical wavelength $\lambda_z = 30$ m as Beaird et al. (2012) is used.

Isotropic turbulence spectra (12) provide vertical velocity variance

$$\langle w^2 \rangle = 5.5(2\pi)^{-2}\varepsilon^{2/3}\int_{m_1}^{m_2} m^{-5/3}dm, \qquad (19)$$

where m_1 and m_2 are minimum and maximum vertical wavenumbers. We assume that isotropic turbulent w dominates, even slightly below the Ozmidov wavenumber (Fig. 13). Applying an isotropic turbulence spectrum and substituting (19), $m_1 = n_1 m_O$ and $m_2 = n_2 m_O$, expressed in terms of the Ozmidov wavenumber m_O, into (16),

$$c = \frac{1.4}{n_1^{-2/3} - n_2^{-2/3}}, \qquad (20)$$

suggesting that the coefficient c depends on the measured wavenumber band relative to m_O.

In analyses by Beaird et al. (2012), $m_O \sim 0.2$ cpm, $m_1 = 1/30$ cpm, and $m_2 \sim 0.5$ cpm, i.e., $n_1 \sim 0.17$ and $n_2 \sim 2.5$, so $c = 0.51$ is expected. This value is close to, but above, their least squares fitting $c = 0.37$. In analyses by Moum (1996), $m_O \sim 0.5$ cpm, $m_1 \sim 1/3.75$ cpm, and $m_2 \sim 10$ cpm, i.e., $n_1 \sim 0.53$ and $n_2 \sim 20$. The predicted coefficient $c = 1.0$ is also close to their least squares fitting $c = 0.73$. In our data, $m_O \sim 1$ cpm (Fig. 11), $m_1 \sim 1/30$ cpm, and $m_2 \sim 1/8$ cpm, i.e., $n_1 \sim 1/3$ and $n_2 \sim 1.25$, so $c = 0.87$ is expected, which is about a half of our least squares fitting $c = 1.9$. Our analysis may require c greater than (20) because the energy-containing scale of turbulence (~the Ozmidov scale) was not always resolved.

Ensemble-mean profiles obtained from the large-eddy parameterization $\langle \varepsilon_{\mathrm{LE}} \rangle$ are reasonably consistent with microstructure $\langle \varepsilon_{\mathrm{micro}} \rangle$ with $R = 0.67$ (Fig. 15). The parameterization tends to overestimate at 100–300-m depths in the western deployment where shear and turbulent dissipation are enhanced, while underestimating below 300 m in the eastern deployment where shear and dissipation are modest (Figs. 8 and 15). This may be explained by our fixed value of c being biased large to account for turbulent vertical velocity variances not resolved by EM-APEX floats for weaker turbulence.

c. Reduced-shear parameterization

Kunze et al. (1990) proposed a parameterization based on reduced shear $|\mathbf{v}_z| - 2N$ which is applicable for data with sufficient vertical resolution and number of observations to capture the statistics of shear instability. The parameterization assumes that (i) temporally or spatially averaged turbulent dissipation is controlled by intermittent shear instability, (ii) instabilities extract the amount of energy needed to decrease the reduced shear $|\mathbf{v}_z| - 2N$ below zero, a shear-stable state (Thorpe 1973; Thompson 1980), and (iii) instability growth rate is that of KH billows. It has been validated in the equatorial Pacific (Peters et al. 1995), at midlatitude (Polzin 1996) and in the Columbia River plume (Jurisa et al. 2016). For the present data, application of this parameterization is promising because EM-APEX floats capture shear-unstable events with reduced shear $|\mathbf{v}_z| - 2N > 0$ in 24% of the total available profiles (Figs. 8a,b and 16b,d).

The reduced-shear parameterization (Kunze et al. 1990) predicts ensemble-average dissipation rate

$$\langle \varepsilon(z) \rangle_{\mathrm{RS}} = \frac{1}{M}\sum_{n=1}^{M}[\delta E(z)\sigma H(V_z^2 - 4N^2)], \qquad (21)$$

where M is the total number of depth intervals, $V_z^2 = u_z^2 + v_z^2$ and N^2 are 4-m vertical shear and stratification, and

$$\delta E(z) = \frac{\delta h^2(\langle u_z \rangle_c^2 + \langle v_z \rangle_c^2 - 4\langle N^2 \rangle_c)}{24} \qquad (22)$$

is the excess kinetic energy available for turbulent production, which is only nonzero in unstable layers satisfying

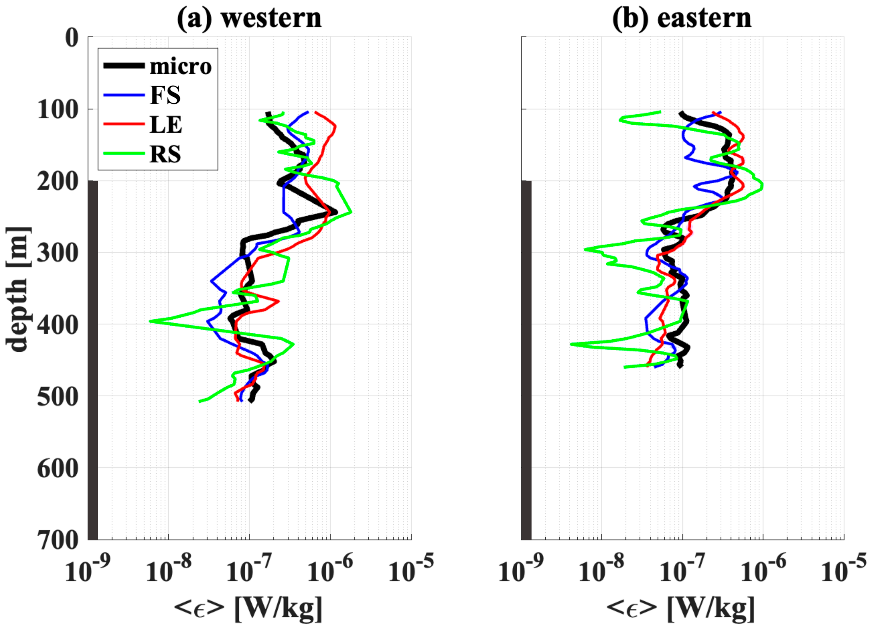

FIG. 15. Vertical profiles of ensemble-average dissipation rates $\langle \varepsilon \rangle$ from the finescale parameterization (FS; blue), large-eddy parameterization (LE; red), reduced-shear parameterization (RS; green), and microstructure measurements (micro; black) for the (a) western and (b) eastern trajectories, respectively. To see downstream conditions more clearly, data north of 30.05°N in the western trajectory and 30°N in the eastern trajectory are excluded from the comparison. Each ensemble-average profile is smoothed over 16-m depth intervals to preserve vertical structure. The 95% confidence intervals of the ensemble-average dissipation rates are not visible because they are smaller than the linewidth. Black vertical bars on the left axes indicate the approximate height of Hirase.

$(V_z^2 - 4N^2) > 0$ in (21) as ensured by the Heaviside function $H(V_z^2 - 4N^2)$. The term δh is the unstable layer thickness,

$$\sigma = \frac{|\mathbf{V}_z| - 2\sqrt{|N^2|}(N^2/|N^2|)}{4} \qquad (23)$$

is the KH instability growth rate (Hazel 1972), and $\langle\rangle_c$ denotes the average over each unstable layer.

The reduced-shear parameterization can be applied only to shear-unstable layers which are intermittent and not always resolved. This is contrary to the finescale parameterization which is applied to larger scales by assuming the energy cascade to microscale by different processes, weak wave–wave interactions. Because only a limited number of unstable events are captured, we focus on the ensemble-average vertical profiles to compare the reduced-shear estimates with those from microstructure and the other parameterizations.

Parameterization (21) is applied to EM-APEX horizontal velocity and density profiles to obtain $\langle \varepsilon \rangle_{\mathrm{RS}}$ as a function of depth for the western and eastern trajectories for comparison with average microstructure profiles $\langle \varepsilon \rangle_{\mathrm{micro}}$. The $\langle \varepsilon \rangle_{\mathrm{RS}}$ is only calculated below the mixed layer ($z > 100$ m) and in the 4-m depth intervals where the total number of available profiles exceeds 50.

Reduced-shear and microstructure estimates of $\langle \varepsilon \rangle$ are consistent (Fig. 15), suggesting that EM-APEX floats satisfactorily capture unstable shear layers in Tokara Strait. The correlation $R = 0.80$ is higher than for large-eddy ($R = 0.67$) and finescale ($R = 0.62$) parameterizations. In the western trajectory, unstable shears were most frequently observed at ~150- and ~250-m depths with 5–10-m thicknesses ~1.5–2 times thinner than in the deeper layer (Fig. 16a). In the eastern trajectory, unstable shears were frequently observed at ~200- and ~400-m depths, where they have similar 10–15-m thicknesses (Fig. 16c). In both trajectories, KH growth rates are ~2 times higher and available unstable energy more than 4 times greater in the shallower layer than in the deeper layer, which results in more elevated turbulent dissipation in the shallower layer (Figs. 16b,d).

8. Conclusions

EM-APEX profiling float and ADCP mooring observations were used to examine energetic fine- and microstructure downstream of ~10-km-wide Hirase Seamount in the path of the Kuroshio in Tokara Strait (Fig. 1). Horizontal and vertical scales of Hirase Seamount, background velocity (Fig. 2), and stratification (Fig. 3) suggest that upstream flows will split

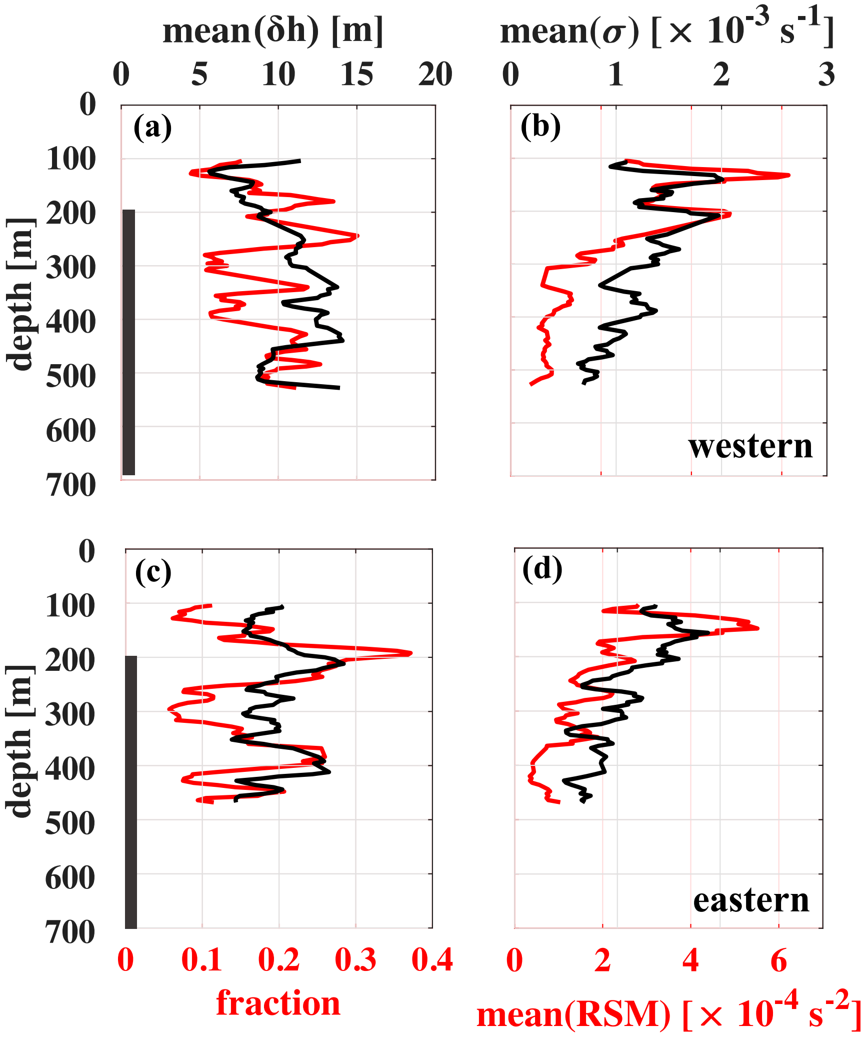

FIG. 16. Vertical profiles of the components of the reduced-shear parameterization (21) for the (bottom) eastern and (top) western trajectories: (a),(c) fraction of shear-unstable data (red) and ensemble-average thickness of unstable shear layers δh (black) and (b),(d) ensemble-average reduced-shear magnitude RSM = $\langle u_z \rangle_c^2 + \langle v_z \rangle_c^2 - 4\langle N^2 \rangle_c$ (red) and Kelvin–Helmholtz instability growth rates σ (black). To reveal downstream conditions more clearly, data north of 30.05°N in the western trajectory and 30°N in the eastern trajectory are excluded from the comparison. Black vertical bars along the left axes indicate the approximate height of Hirase.

around the seamount and vertically sheared vortices will form in the downstream wake of the seamount flanks (e.g., Baines 1995; Srinivasan et al. 2021), consistent with EM-APEX float profile sections (Fig. 4). Conventional upgoing lee-wave generation will be confined to the summit crown. Mooring frequency spectra of vertical shear have broadband spectral enhancement from subinertial to supertidal at 100–300-m depth downstream (Fig. 5).

The EM-APEX floats capture energetic turbulence above the seamount flanks and extending downstream (i) for at least 20 km in a layer spanning 150–250-m depth in the pycnocline where TKE dissipation rates $\varepsilon \sim \mathcal{O}(10^{-6})$ W kg^{-1} and diapycnal diffusivities $K \sim \mathcal{O}(10^{-2})$ m^2 s^{-1}, and (ii) for 10 km downstream at ~350–450-m depth where $\varepsilon \sim \mathcal{O}(10^{-7})$ W kg^{-1} and $K \sim \mathcal{O}(10^{-2})$ m^{2}s^{-1} (Fig. 6). The strongest turbulence is associated with 4-m reduced shear $|\mathbf{v}_z|^2 - 4N^2 > 0$ (Fig. 7), indicating shear instability. Float and mooring time series suggest that shear instability is associated with intermittent patches of both enhanced shear and reduced stratification (Figs. 8 and 9).

Previous measurements indicate that layers of elevated turbulence extend at least 100 km downstream of Hirase (Nagai et al. 2017, 2019, 2021; Hasegawa et al. 2021). That turbulence extends farther downstream than expected for turbulent decay times $\mathcal{O}(N^{-1})$ (Ozmidov 1965) and background (Kuroshio and tidal) current speeds suggests continuous replenishment. There are several possible mechanisms for continuous replenishment of turbulence: (i) local nonlinear instability of marginally unstable wake vortices (e.g., Thomas et al. 2013; Nagai et al. 2021), (ii) nonlocal anisotropic stratified turbulence generated at the seamount which can sustain isotropic turbulence downstream for time scales of (1–10)f^{-1} (Kunze 2019), and (iii) for the 150–250-m depth layer, lee-wave trapping at vertical critical layers at the base of the Kuroshio (Fig. 10). Mechanisms (i) and (iii) involve local generation of turbulence while (ii) involves anisotropic turbulence generation at the seamount and advection downstream. Since ray tracing suggests that none of the lee waves reach 400-m depth, the elevated turbulence in this layer could be caused by (i) or (ii) associated with shed frictional bottom layers (Hasegawa et al. 2021) or tidal vortices (Inoue et al. 2024).

Vertical wavenumber spectra for vertical shear, strain, and vertical divergence (Fig. 11) are orders of magnitude higher than canonical GM levels (Garrett and Munk 1975; Cairns and Williams 1976; Gregg and Kunze 1991; Thurnherr et al. 2015). Shear and strain spectra are saturated with spectral levels invariant with ε, $|\mathbf{v}_z| \sim N$, and spectral slopes of ~ -1 for vertical wavenumbers as low as 0.01 cpm, suggesting that flows are nonlinear on scales comparable to water depths (Figs. 11a,b). In contrast, vertical divergence spectral levels increase with increasing ε (Fig. 11c). Spectral amplitudes of vertical kinetic energy are comparable to those of horizontal kinetic energy at 10-m vertical scales for the strongest dissipation rates, signifying isotropy and consistent with the measurements resolving the Ozmidov length (Fig. 12). Observed vertical divergence w_z is consistent with the GM model (Thurnherr et al. 2015) at 100-m vertical scales, while agreeing with the transition between anisotropic turbulence (Kunze 2019) and isotropic turbulence (Kolmogorov 1941; Batchelor 1953; Ozmidov 1965; Tennekes and Lumley 1972; Thorpe 2005) at 10-m vertical scales (Fig. 13).

Measured ε correlates well with finescale (Gregg 1989; Polzin et al. 1995; Gregg et al. 2003), large-eddy (Moum 1996; D'Asaro and Lien 2000b), and reduced-shear (Kunze et al. 1990) parameterizations ranging from the roll-off length scales of weakly nonlinear internal waves (~100 m in this case) to the Ozmidov length scales of isotropic turbulence (~10 m for the strongest turbulence) (Figs. 14–16). The large-eddy scaling appears to work even though the Ozmidov scales are not fully resolved. The lee of Hirase is close to the wave–turbulence transition (D'Asaro and Lien 2000b) with the saturated spectrum (anisotropic stratified turbulence) extending to vertical length scales as large as 100 m, comparable to the water depth in Tokara Strait.

Extensive EM-APEX float measurements in this study demonstrate relationships between microstructure and vertical fine structure. Flow–topography interaction theory suggests the vertical fine structure contains lee waves and submesoscale vortical motions with similar temporal and spatial scales. The two could not be distinguished in the present 2D measurements using the float's line array because PV could not be estimated. Future 3D measurements and numerical simulations may allow identification of turbulence generation mechanisms on the seamount flanks and downstream more rigorously. Time-evolving tidal currents may make the Kuroshio–seamount interactions more complex (e.g., MacKinnon et al. 2019; Inoue et al. 2024), which could be addressed with 3D numerical simulations and long-term mooring observations.

Acknowledgments. The authors are grateful to the crew and officers of the TRV *Kagoshima-maru*, as well as all November 2019 cruise participants for their assistance. Special thanks go to Avery Snyder, Takeshi Matsuno, Toru Kobari, and Akie Sakai. Sebastian Essink helped with FP07 data analysis. We also appreciate an anonymous reviewer for insightful comments. This work was supported by the National Science Foundation Grants OCE-1829082 and OCE-1829190 and Japan Society for the Promotion of Science KAKENHI Grants JP15H05818 and JP15H05821.

Data availability statement. The EM-APEX float and ADCP mooring data are available at http://hdl.handle.net/1773/49468. ETOPO1 bathymetry data are distributed by NOAA National Geophysical Data Center (https://www.ncei.noaa.gov/access/metadata/landing-page/bin/iso?id=gov.noaa.ngdc.mgg.dem:316). Global Ocean Physics Reanalysis data are distributed by CMEMS (https://resources.marine.copernicus.eu/product-detail/GLOBAL_MULTIYEAR_PHY_001_030).

APPENDIX A

Background Density Profiles from EM-APEX Floats

Stable background density profiles for the western and eastern float trajectories are constructed separately, using all EM-APEX float profiles along these two trajectories. For each deployment, a total of N_{tot} density points were measured from all floats with vertical resolution $\Delta z = 2$ m to maximum depth $H_{\max} = M\Delta z$. For each depth interval $(i-1)\Delta z < z < i\Delta z$ $(i = 2, \ldots, M)$, a finer vertical interval is defined $\delta z_i = \Delta z/n_i$, where n_i is the total number of data points in this depth interval such that $\sum_{i=2}^{M} n_i = N_{\text{tot}}$. The new depth grid has variable intervals δz_i, and consists of N_{tot} points running from 0 to $H_{\max}$ with finer resolution where there are more samples and coarser as z approaches $H_{\max}$. In other words, all CTD measurements during each line-array deployment are used to construct a single vertical profile with variable finer vertical resolution at different depths according to the number of data points collected in each depth interval. Then the N_{tot} data samples are sorted by potential density σ_0 and stored in the new scaled depths. The resulting sorted density profile is subsampled at the original depth grid Δz and referred to as the background density σ_0^{BG} profile (Fig. 3a). Background stratification N_{BG}^2 (Fig. 3b) is computed from the vertical gradient of background potential density profile and smoothed over 40 m.

APPENDIX B

Quality Control of Microstructure Data

The data quality of microstructure thermal-variance dissipation rate χ is often evaluated by the degree of agreement

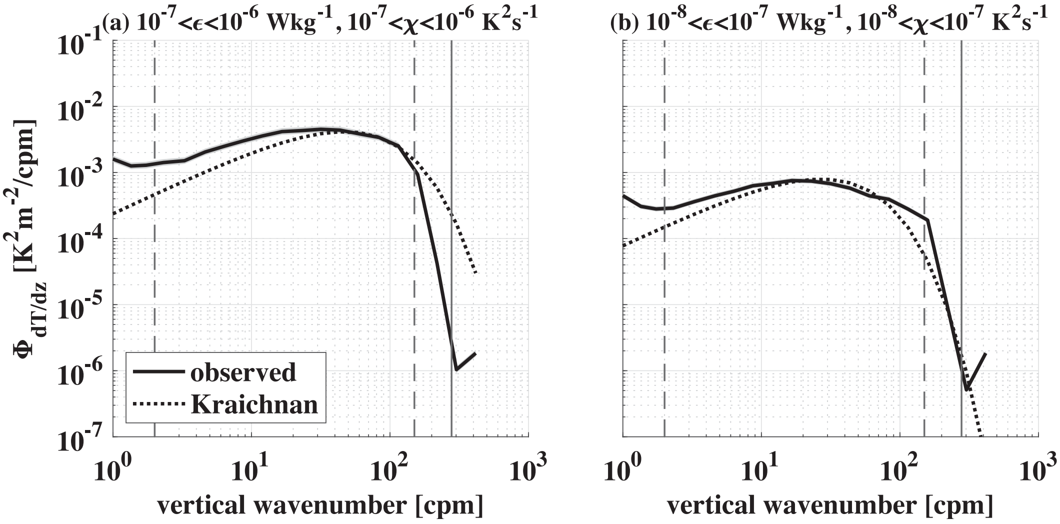

FIG. B1. Comparison between measured (solid lines) and Kraichnan universal temperature gradient spectrum (dotted lines), both averaged for data with dissipation rates ε and χ shown above the upper axes. Dashed vertical lines indicate minimum ($k_z^{\min} = 2$ cpm) and maximum vertical wavenumbers ($k_z^{\max} = 150$ cpm) used for spectral integration; solid vertical lines indicate the average Batchelor wavenumber k_B. The 95% confidence intervals are invisible because they are within the width of lines.

between measured temperature-gradient vertical wavenumber spectrum $\Phi_{\partial_z T}$ (see section 2d) and corresponding theoretical universal spectrum (Batchelor 1959; Kraichnan 1968). In this study, the Kraichnan universal spectrum as expressed by Roget et al. (2006)

$$\Phi^{\mathrm{univ}}_{\partial_z T}(k_z) = \frac{\chi q_K^{1/2} y_k \exp\left(-\sqrt{6}\, y_k\right)}{\kappa_T k_B} \tag{B1}$$

is used where $q_K = 5.26$ is the Kraichnan constant (Bogucki et al. 1997, 2012; Peterson and Fer 2014; Goto et al. 2016), $y_k = \sqrt{q_k}\, k_z / k_B$, κ_T the molecular thermal diffusivity, and

$$k_B = (2\pi)^{-1}(\nu \kappa_T^2/\varepsilon)^{-1/4} \tag{B2}$$

the Batchelor wavenumber (cpm) with the kinematic viscosity ν and TKE dissipation rate ε.

Figure B1 compares composite temperature gradient spectra with the corresponding Kraichnan universal spectra, both calculated for each ε and χ value. Measured spectra tend to be slightly higher than the Kraichnan spectra at lower k_z, but the shapes are similar. In this study, the ratio of the observed to Kraichnan spectrum integrated over the vertical wavenumber band $k_z^{\min} < k_z < k_z^{\max}$ in (6),

$$R_{\mathrm{qc}} = \frac{\displaystyle\int_{k_z^{\min}}^{k_z^{\max}} \Phi_{\partial_z T}(k_z)\, dk_z}{\displaystyle\int_{k_z^{\min}}^{k_z^{\max}} \Phi^{\mathrm{univ}}_{\partial_z T}(k_z)\, dk_z}, \tag{B3}$$

is used for quality control of χ. Data with $0.5 < R_{\mathrm{qc}} < 2$ are included in the analysis.

APPENDIX C

Ray Tracing of Lee Waves in the Kuroshio Shear

Propagating lee waves are generated by Kuroshio flow $U(z) > 0$ for along-stream horizontal wavenumbers satisfying $f/U < |k| < N/U$ where k is the topographic wavenumber and corresponds to upstream phase propagation equal and opposite to U. Lee-wave intrinsic frequencies following water motion obey the internal-wave dispersion relation

$$\hat{\omega} = -kU = \sqrt{\frac{f^2 m^2 + N^2 k^2}{m^2 + k^2}} \tag{C1}$$

so that the vertical wavenumber is

$$m = \pm k \sqrt{\frac{N^2 - k^2 U^2}{k^2 U^2 - f^2}}. \tag{C2}$$

The Eulerian along-stream group velocity is

$$Cg_{xE} = U + Cg_{xL} = \frac{N^2 f^2 + (k^2 U^2)^2 - k^2 U^2 f^2}{N^2 (kU) k}, \tag{C3}$$

which is U for $|kU| \to f$ and $|kU| \to N$, and ~ 0 for $f \ll |kU| \ll N$. The vertical group velocity

$$Cg_z = \frac{(N^2 - k^2 U^2)^{1/2} (k^2 U^2 - f^2)^{3/2}}{N^2 (kU) k}. \tag{C4}$$

Ray paths are calculated using the method of characteristics

$$dx = \frac{Cg_{xE}}{Cg_z} dz = \frac{N^2 f^2 + (k^2 U^2)^2 - k^2 U^2 f^2}{(N^2 - k^2 U^2)^{1/2} (k^2 U^2 - f^2)^{3/2}} dz. \tag{C5}$$

Along-stream wavenumber k is set at its initial bottom condition at the summit and is invariant assuming that the background flow U and buoyancy frequency N are functions only of depth z. Polynomial fits to the observed ensemble-average profiles of U and N (Fig. 10b) are used for the ray tracing. Initial conditions at the summit $(x, z) = (0, 2000\ \mathrm{m})$ include all propagating lee-wave wavenumbers $|f/U_0| < k < |N/U_0|$, where $U_0 \sim 0.5\ \mathrm{m\ s^{-1}}$ and $N_0 \sim 10^{-2}\ \mathrm{s^{-1}}$ are the flow and stratification at the summit depth.

In (C5), vertical increment is set as $dz = 1$ m if the resulting horizontal increment $dx < 10$ m, otherwise horizontal increment $dx = 10$ m is used. Rays are terminated (i) if they fall 20 m below the bottom (gray shading in Fig. 10a), (ii) if they leave the domain ($x > 20$ km), or (iii) if the vertical wavenumber magnitude $|m|$ exceeds 0.1 cpm.

REFERENCES

Althaus, A. M., E. Kunze, and T. B. Sanford, 2003: Internal tide radiation from Mendocino escarpment. *J. Phys. Oceanogr.*, **33**, 1510–1527, https://doi.org/10.1175/1520-0485(2003)033<1510:ITRFME>2.0.CO;2.

Baines, P. G., 1995: *Topographic Effects in Stratified Flows*. Cambridge University Press, 482 pp.

Baker, L., and A. Mashayek, 2021: Surface reflection of bottom generated oceanic lee waves. *J. Fluid Mech.*, **924**, A17, https://doi.org/10.1017/jfm.2021.627.

Balmforth, N. J., G. R. Ierley, and W. R. Young, 2002: Tidal conversion by subcritical topography. *J. Phys. Oceanogr.*, **32**, 2900–2914, https://doi.org/10.1175/1520-0485(2002)032%3C2900:TCBST%3E2.0.CO;2.

Batchelor, G. K., 1953: *The Theory of Homogeneous Turbulence*. Cambridge University Press, 197 pp.

——, 1959: Small-scale variation of convected quantities like temperature in turbulent fluid Part 1. General discussion and the case of small conductivity. *J. Fluid Mech.*, **5**, 113–133, https://doi.org/10.1017/S002211205900009X.

Beaird, N., I. Fer, P. Rhines, and C. Eriksen, 2012: Dissipation of turbulent kinetic energy inferred from Seagliders: An application to the eastern Nordic Seas overflows. *J. Phys. Oceanogr.*, **42**, 2268–2282, https://doi.org/10.1175/JPO-D-12-094.1.

Bell, T. H., 1975a: Lee waves in stratified flows with simple harmonic time dependence. *J. Fluid Mech.*, **67**, 705–722, https://doi.org/10.1017/S0022112075000560.

Bell, T. H., Jr., 1975b: Topographically generated internal waves in the open ocean. *J. Geophys. Res.*, **80**, 320–327, https://doi.org/10.1029/JC080i003p00320.

Bogucki, D., J. A. Domaradzki, and P. K. Yeung, 1997: Direct numerical simulations of passive scalars with $Pr{>}1$ advected by turbulent flow. *J. Fluid Mech.*, **343**, 111–130, https://doi.org/10.1017/S0022112097005727.

Bogucki, D. J., H. Luo, and J. A. Domaradzki, 2012: Experimental evidence of the Kraichnan scalar spectrum at high Reynolds numbers. *J. Phys. Oceanogr.*, **42**, 1717–1728, https://doi.org/10.1175/JPO-D-11-0214.1.

Burchard, H., O. Petersen, and T. P. Rippeth, 1998: Comparing the performance of the Mellor-Yamada and the κ-ϵ two-equation turbulence models. *J. Geophys. Res.*, **103**, 10 543–10 554, https://doi.org/10.1029/98JC00261.

Cairns, J. L., and G. O. Williams, 1976: Internal wave observations from a midwater float, 2. *J. Geophys. Res.*, **81**, 1943–1950, https://doi.org/10.1029/JC081i012p01943.

Caldeira, R. M. A., A. Stegner, X. Couvelard, I. B. Araújo, P. Testor, and A. Lorenzo, 2014: Evolution of an oceanic anticyclone in the lee of Madeira Island: In situ and remote sensing survey. *J. Geophys. Res. Oceans*, **119**, 1195–1216, https://doi.org/10.1002/2013JC009493.

Carter, G. S., and M. C. Gregg, 2002: Intense, variable mixing near the head of Monterey Submarine Canyon. *J. Phys. Oceanogr.*, **32**, 3145–3165, https://doi.org/10.1175/1520-0485(2002)032<3145:IVMNTH>2.0.CO;2.

Chang, M.-H., T. Y. Tang, C.-R. Ho, and S.-Y. Chao, 2013: Kuroshio-induced wake in the lee of Green Island off Taiwan. *J. Geophys. Res. Oceans*, **118**, 1508–1519, https://doi.org/10.1002/jgrc.20151.

——, S.-Y. Jheng, and R.-C. Lien, 2016: Trains of large Kelvin-Helmholtz billows observed in the Kuroshio above a seamount. *Geophys. Res. Lett.*, **43**, 8654–8661, https://doi.org/10.1002/2016GL069462.

——, S. Jan, C.-L. Liu, Y.-H. Cheng, and V. Mensah, 2019: Observations of island wakes at high Rossby numbers: Evolution of submesoscale vortices and free shear layers. *J. Phys. Oceanogr.*, **49**, 2997–3016, https://doi.org/10.1175/JPO-D-19-0035.1.

Codiga, D. L., 2011: Unified tidal analysis and prediction using the UTide Matlab functions. Graduate School of Oceanography–University of Rhode Island Tech. Rep. 2011-01, 59 pp.

Cusack, J. M., A. C. Naveira Garabato, D. A. Smeed, and J. B. Girton, 2017: Observation of a large lee wave in the Drake Passage. *J. Phys. Oceanogr.*, **47**, 793–810, https://doi.org/10.1175/JPO-D-16-0153.1.

D'Asaro, E. A., 1988: Generation of submesoscale vortices: A new mechanism. *J. Geophys. Res.*, **93**, 6685–6693, https://doi.org/10.1029/JC093iC06p06685.

——, and R.-C. Lien, 2000a: Lagrangian measurements of waves and turbulence in stratified flows. *J. Phys. Oceanogr.*, **30**, 641–655, https://doi.org/10.1175/1520-0485(2000)030<0641:LMOWAT>2.0.CO;2.

——, and ——, 2000b: The wave–turbulence transition for stratified flows. *J. Phys. Oceanogr.*, **30**, 1669–1678, https://doi.org/10.1175/1520-0485(2000)030%3C1669:TWTTFS%3E2.0.CO;2.

Desaubies, Y. J. F., 1975: A linear theory of internal wave spectra and coherences near the Väisälä frequency. *J. Geophys. Res.*, **80**, 895–899, https://doi.org/10.1029/JC080i006p00895.

Dewan, E. M., 1979: Stratospheric wave spectra resembling turbulence. *Science*, **204**, 832–835, https://doi.org/10.1126/science.204.4395.832.

Eriksen, C. C., 1982: Observations of internal wave reflection off sloping bottoms. *J. Geophys. Res.*, **87**, 525–538, https://doi.org/10.1029/JC087iC01p00525.

——, 1998: Internal wave reflection and mixing at Fieberling Guyot. *J. Geophys. Res.*, **103**, 2977–2994, https://doi.org/10.1029/97JC03205.

Essink, S., E. Kunze, R.-C. Lien, R. Inoue, and S.-I. Ito, 2022: Near-inertial wave interactions and turbulence production in a Kuroshio anticyclonic eddy. *J. Phys. Oceanogr.*, **52**, 2687–2704, https://doi.org/10.1175/JPO-D-21-0278.1.

Evans, D. G., and Coauthors, 2018: Annual cycle of turbulent dissipation estimated from Seagliders. *Geophys. Res. Lett.*, **45**, 10 560–10 569, https://doi.org/10.1029/2018GL079966.

Farmer, D., and L. Armi, 1999: Stratified flow over topography: The role of small-scale entrainment and mixing in flow establishment. *Proc. Roy. Soc. London*, **455A**, 3221–3258, https://doi.org/10.1098/rspa.1999.0448.

Frajka-Williams, E., C. C. Eriksen, P. B. Rhines, and R. R. Harcourt, 2011: Determining vertical water velocities from Seaglider. *J. Atmos. Oceanic Technol.*, **28**, 1641–1656, https://doi.org/10.1175/2011JTECHO830.1.

Gargett, A. E., 1990: Do we really know how to scale the turbulent kinetic energy dissipation rate ϵ due to breaking of oceanic internal waves? *J. Geophys. Res.*, **95**, 15 971–15 974, https://doi.org/10.1029/JC095iC09p15971.

——, P. J. Hendricks, T. B. Sanford, T. R. Osborn, and A. J. Williams, 1981: A composite spectrum of vertical shear in the upper ocean. *J. Phys. Oceanogr.*, **11**, 1258–1271, https://doi.org/10.1175/1520-0485(1981)011<1258:ACSOVS>2.0.CO;2.

Garrett, C., and W. Munk, 1975: Space-time scales of internal waves: A progress report. *J. Geophys. Res.*, **80**, 291–297, https://doi.org/10.1029/JC080i003p00291.

——, and ——, 1979: Internal waves in the ocean. *Annu. Rev. Fluid Mech.*, **11**, 339–369, https://doi.org/10.1146/annurev.fl.11.010179.002011.

——, and E. Kunze, 2007: Internal tide generation in the deep ocean. *Annu. Rev. Fluid Mech.*, **39**, 57–87, https://doi.org/10.1146/annurev.fluid.39.050905.110227.

Goto, Y., I. Yasuda, and M. Nagasawa, 2016: Turbulence estimation using fast-response thermistors attached to a free-fall vertical microstructure profiler. *J. Atmos. Oceanic Technol.*, **33**, 2065–2078, https://doi.org/10.1175/JTECH-D-15-0220.1.

Gregg, M. C., 1989: Scaling turbulent dissipation in the thermocline. *J. Geophys. Res.*, **94**, 9686–9698, https://doi.org/10.1029/JC094iC07p09686.

——, and E. Kunze, 1991: Shear and strain in Santa Monica Basin. *J. Geophys. Res.*, **96**, 16 709–16 719, https://doi.org/10.1029/91JC01385.

——, T. B. Sanford, and D. P. Winkel, 2003: Reduced mixing from the breaking of internal waves in equatorial waters. *Nature*, **422**, 513–515, https://doi.org/10.1038/nature01507.

——, E. A. D'Asaro, J. J. Riley, and E. Kunze, 2018: Mixing efficiency in the ocean. *Annu. Rev. Mar. Sci.*, **10**, 443–473, https://doi.org/10.1146/annurev-marine-121916-063643.

Guo, X., X.-H. Zhu, Q.-S. Wu, and D. Huang, 2012: The Kuroshio nutrient stream and its temporal variation in the East China Sea. *J. Geophys. Res.*, **117**, C01026, https://doi.org/10.1029/2011JC007292.

Guo, X. Y., X.-H. Zhu, Y. Long, and D. J. Huang, 2013: Spatial variations in the Kuroshio nutrient transport from the East China Sea to South of Japan. *Biogeosciences*, **10**, 6403–6417, https://doi.org/10.5194/bg-10-6403-2013.

Hasegawa, D., and Coauthors, 2021: How a small reef in the Kuroshio cultivates the ocean. *Geophys. Res. Lett.*, **48**, e2020GL092063, https://doi.org/10.1029/2020GL092063.

Hazel, P., 1972: Numerical studies of the stability of inviscid stratified shear flows. *J. Fluid Mech.*, **51**, 39–61, https://doi.org/10.1017/S0022112072001065.

Henyey, F. S., J. Wright, and S. M. Flatté, 1986: Energy and action flow through the internal wave field: An eikonal approach. *J. Geophys. Res.*, **91**, 8487–8495, https://doi.org/10.1029/JC091iC07p08487.

Hibiya, T., N. Furuichi, and R. Robertson, 2012: Assessment of fine-scale parameterizations of turbulent dissipation rates near mixing hotspots in the deep ocean. *Geophys. Res. Lett.*, **39**, L24601, https://doi.org/10.1029/2012GL054068.

Inoue, R., E. Tsutsumi, and H. Nakamura, 2024: Numerical simulation of the Kuroshio flowing over the Hirase Seamount in the Tokara Strait in autumn: Tidal vortex shedding in a baroclinic jet. *J. Phys. Oceanogr.*, **54**, 153–172, https://doi.org/10.1175/JPO-D-23-0050.1.

Johnston, T. M. S., and Coauthors, 2019: Energy and momentum lost to wake eddies and lee waves generated by the North Equatorial Current and tidal flows at Peleliu, Palau. *Oceanography*, **32**, 110–125, https://doi.org/10.5670/oceanog.2019.417.

Jurisa, J. T., J. D. Nash, J. N. Moum, and L. F. Kilcher, 2016: Controls on turbulent mixing in a strongly stratified and sheared tidal river plume. *J. Phys. Oceanogr.*, **46**, 2373–2388, https://doi.org/10.1175/JPO-D-15-0156.1.

Klymak, J. M., and M. C. Gregg, 2004: Tidally generated turbulence over the Knight Inlet sill. *J. Phys. Oceanogr.*, **34**, 1135–1151, https://doi.org/10.1175/1520-0485(2004)034%3C1135:TGTOTK%3E2.0.CO;2.

——, R. Pinkel, and L. Rainville, 2008: Direct breaking of the internal tide near topography: Kaena Ridge, Hawaii. *J. Phys. Oceanogr.*, **38**, 380–399, https://doi.org/10.1175/2007JPO3728.1.

Kolmogorov, A., 1941: The local structure of turbulence in incompressible viscous fluids for very large Reynolds number. *Dokl. Akad. Nauk SSSR*, **30**, 199–303.

Kraichnan, R. H., 1968: Small-scale structure of a scalar field convected by turbulence. *Phys. Fluids*, **11**, 945–953, https://doi.org/10.1063/1.1692063.

Kunze, E., 1985: Near-inertial wave propagation in geostrophic shear. *J. Phys. Oceanogr.*, **15**, 544–565, https://doi.org/10.1175/1520-0485(1985)015%3C0544:NIWPIG%3E2.0.CO;2.

——, 2017: Internal-wave-driven mixing: Global geography and budgets. *J. Phys. Oceanogr.*, **47**, 1325–1345, https://doi.org/10.1175/JPO-D-16-0141.1.

——, 2019: A unified model spectrum for anisotropic stratified and isotropic turbulence in the ocean and atmosphere. *J. Phys. Oceanogr.*, **49**, 385–407, https://doi.org/10.1175/JPO-D-18-0092.1.

——, and J. M. Toole, 1997: Tidally driven vorticity, diurnal shear, and turbulence atop Fieberling Seamount. *J. Phys. Oceanogr.*, **27**, 2663–2693, https://doi.org/10.1175/1520-0485(1997)027<2663:TDVDSA>2.0.CO;2.

——, and R.-C. Lien, 2019: Energy sinks for lee waves in shear flow. *J. Phys. Oceanogr.*, **49**, 2851–2865, https://doi.org/10.1175/JPO-D-19-0052.1.

——, A. J. Williams III, and M. G. Briscoe, 1990: Observations of shear and vertical stability from a neutrally buoyant float. *J. Geophys. Res.*, **95**, 18 127–18 142, https://doi.org/10.1029/JC095iC10p18127.

——, R. W. Schmitt, and J. M. Toole, 1995: The energy balance in a warm-core ring's near-inertial critical layer. *J. Phys. Oceanogr.*, **25**, 942–957, https://doi.org/10.1175/1520-0485(1995)025<0942:TEBIAW>2.0.CO;2.

——, L. K. Rosenfeld, G. S. Carter, and M. C. Gregg, 2002: Internal waves in Monterey Submarine Canyon. *J. Phys. Oceanogr.*, **32**, 1890–1913, https://doi.org/10.1175/1520-0485(2002)032<1890:IWIMSC>2.0.CO;2.

——, E. Firing, J. M. Hummon, T. K. Chereskin, and A. M. Thurnherr, 2006: Global abyssal mixing inferred from lowered ADCP shear and CTD strain profiles. *J. Phys. Oceanogr.*, **36**, 1553–1576, https://doi.org/10.1175/JPO2926.1.

——, C. MacKay, E. E. McPhee-Shaw, K. Morrice, J. B. Girton, and S. R. Terker, 2012: Turbulent mixing and exchange with interior waters on sloping boundaries. *J. Phys. Oceanogr.*, **42**, 910–927, https://doi.org/10.1175/JPO-D-11-075.1.

Legg, S., 2021: Mixing by oceanic lee waves. *Annu. Rev. Fluid Mech.*, **53**, 173–201, https://doi.org/10.1146/annurev-fluid-051220-043904.

Lien, R.-C., and T. B. Sanford, 2019: Small-scale potential vorticity in the upper-ocean thermocline. *J. Phys. Oceanogr.*, **49**, 1845–1872, https://doi.org/10.1175/JPO-D-18-0052.1.

——, M. J. McPhaden, and M. C. Gregg, 1996: High-frequency internal waves at 0°, 140°W and their possible relationship to deep-cycle turbulence. *J. Phys. Oceanogr.*, **26**, 581–600, https://doi.org/10.1175/1520-0485(1996)026<0581:HFIWAA>2.0.CO;2.

——, T. B. Sanford, J. A. Carlson, and J. H. Dunlap, 2016: Autonomous microstructure EM-APEX floats. *Methods Oceanogr.*, **17**, 282–295, https://doi.org/10.1016/j.mio.2016.09.003.

Lighthill, M. J., 1978: *Waves in Fluids*. Cambridge University Press, 504 pp.

MacCready, P., and P. B. Rhines, 1993: Slippery bottom boundary layers on a slope. *J. Phys. Oceanogr.*, **23**, 5–22, https://doi.org/10.1175/1520-0485(1993)023%3C0005:SBBLOA%3E2.0.CO;2.

MacKinnon, J. A., and M. C. Gregg, 2005: Spring mixing: Turbulence and internal waves during restratification on the New England Shelf. *J. Phys. Oceanogr.*, **35**, 2425–2443, https://doi.org/10.1175/JPO2821.1.

——, M. H. Alford, G. Voet, K. L. Zeiden, T. M. Shaun Johnston, M. Siegelman, S. Merrifield, and M. Merrifield, 2019: Eddy wake generation from broadband currents near Palau. *J. Geophys. Res. Oceans*, **124**, 4891–4903, https://doi.org/10.1029/2019JC014945.

McComas, C. H., and P. Müller, 1981: The dynamic balance of internal waves. *J. Phys. Oceanogr.*, **11**, 970–986, https://doi.org/10.1175/1520-0485(1981)011%3C0970:TDBOIW%3E2.0.CO;2.

McDougall, T. J., and P. Barker, 2011: Getting started with TEOS-10 and the Gibbs Seawater (GSW) Oceanographic Toolbox. SCOR/IAPSO WG127, 28 pp., http://www.teos-10.org/pubs/Getting_Started.pdf.

Mellor, G. L., and T. Yamada, 1982: Development of a turbulence closure model for geophysical fluid problems. *Rev. Geophys.*, **20**, 851–875, https://doi.org/10.1029/RG020i004p00851.

Mohri, K., T. Hibiya, and N. Iwamae, 2010: Revisiting internal wave generation by tide-topography interaction. *J. Geophys. Res.*, **115**, C11001, https://doi.org/10.1029/2009JC005908.

Molemaker, M. J., J. C. McWilliams, and W. K. Dewar, 2015: Submesoscale instability and generation of mesoscale anticyclones near a separation of the California Undercurrent. *J. Phys. Oceanogr.*, **45**, 613–629, https://doi.org/10.1175/JPO-D-13-0225.1.

Monismith, S. G., J. R. Koseff, and B. L. White, 2018: Mixing efficiency in the presence of stratification: When is it constant? *Geophys. Res. Lett.*, **45**, 5627–5634, https://doi.org/10.1029/2018GL077229.

Moum, J. N., 1996: Energy-containing scales of turbulence in the ocean thermocline. *J. Geophys. Res.*, **101**, 14 095–14 109, https://doi.org/10.1029/96JC00507.

——, and J. D. Nash, 2000: Topographically induced drag and mixing at a small bank on the continental shelf. *J. Phys. Oceanogr.*, **30**, 2049–2054, https://doi.org/10.1175/1520-0485(2000)030<2049:TIDAMA>2.0.CO;2.

Müller, P., and N. Xu, 1992: Scattering of oceanic internal gravity waves off random bottom topography. *J. Phys. Oceanogr.*, **22**, 474–488, https://doi.org/10.1175/1520-0485(1992)022<0474:SOOIGW>2.0.CO;2.

Nagai, T., D. Hasegawa, T. Tanaka, H. Nakamura, E. Tsutsumi, R. Inoue, and T. Yamashiro, 2017: First evidence of coherent bands of strong turbulent layers associated with high-wavenumber internal-wave shear in the upstream Kuroshio. *Sci. Rep.*, **7**, 14555, https://doi.org/10.1038/s41598-017-15167-1.

——, and Coauthors, 2019: How the Kuroshio Current delivers nutrients to sunlit layers on the continental shelves with aid of near-inertial waves and turbulence. *Geophys. Res. Lett.*, **46**, 6726–6735, https://doi.org/10.1029/2019GL082680.

——, and Coauthors, 2021: The Kuroshio flowing over seamounts and associated submesoscale flows drive 100-km-wide 100-1000-fold enhancement of turbulence. *Commun. Earth Environ.*, **2**, 170, https://doi.org/10.1038/s43247-021-00230-7.

Nash, J. D., E. Kunze, J. M. Toole, and R. W. Schmitt, 2004: Internal tide reflection and turbulent mixing on the continental slope. *J. Phys. Oceanogr.*, **34**, 1117–1134, https://doi.org/10.1175/1520-0485(2004)034<1117:ITRATM>2.0.CO;2.

——, ——, C. M. Lee, and T. B. Sanford, 2006: Structure of the baroclinic tide generated at Kaena Ridge, Hawaii. *J. Phys. Oceanogr.*, **36**, 1123–1135, https://doi.org/10.1175/JPO2883.1.

Nasmyth, P. W., 1970: Oceanic turbulence. Ph.D. thesis, University of British Columbia, 69 pp.

Naveira Garabato, A. C., K. L. Polzin, B. A. King, K. J. Heywood, and M. Visbeck, 2004: Widespread intense turbulent mixing in the Southern Ocean. *Science*, **303**, 210–213, https://doi.org/10.1126/science.1090929.

Nikurashin, M., and R. Ferrari, 2010: Radiation and dissipation of internal waves generated by geostrophic motions impinging on small-scale topography: Theory. *J. Phys. Oceanogr.*, **40**, 1055–1074, https://doi.org/10.1175/2009JPO4199.1.

——, ——, N. Grisouard, and K. Polzin, 2014: The impact of finite-amplitude bottom topography on internal wave generation in the Southern Ocean. *J. Phys. Oceanogr.*, **44**, 2938–2950, https://doi.org/10.1175/JPO-D-13-0201.1.

Oakey, N. S., 1982: Determination of the rate of dissipation of turbulent energy from simultaneous temperature and velocity shear microstructure measurements. *J. Phys. Oceanogr.*, **12**, 256–271, https://doi.org/10.1175/1520-0485(1982)012<0256:DOTROD>2.0.CO;2.

Osborn, T. R., 1980: Estimates of the local rate of vertical diffusion from dissipation measurements. *J. Phys. Oceanogr.*, **10**, 83–89, https://doi.org/10.1175/1520-0485(1980)010%3C0083:EOTLRO%3E2.0.CO;2.

——, and C. S. Cox, 1972: Oceanic fine structure. *Geophys. Fluid Dyn.*, **3**, 321–345, https://doi.org/10.1080/03091927208236085.

Ozmidov, R. V., 1965: On the turbulent exchange in a stably stratified ocean. *Izv. Acad. Sci. USSR, Atmos. Oceanic Phys.*, **1**, 853–860.

Perfect, B., N. Kumar, and J. J. Riley, 2018: Vortex structures in the wake of an idealized seamount in rotating, stratified flow. *Geophys. Res. Lett.*, **45**, 9098–9105, https://doi.org/10.1029/2018GL078703.

——, ——, and ——, 2020a: Energetics of seamount wakes. Part I: Energy exchange. *J. Phys. Oceanogr.*, **50**, 1365–1382, https://doi.org/10.1175/JPO-D-19-0105.1.

——, ——, and ——, 2020b: Energetics of seamount wakes. Part II: Wave fluxes. *J. Phys. Oceanogr.*, **50**, 1383–1398, https://doi.org/10.1175/JPO-D-19-0104.1.

Peters, H., M. C. Gregg, and T. B. Sanford, 1995: On the parameterization of equatorial turbulence: Effect of fine-scale variations below the range of the diurnal cycle. *J. Geophys. Res.*, **100**, 18 333–18 348, https://doi.org/10.1029/95JC01513.

Peterson, A. K., and I. Fer, 2014: Dissipation measurements using temperature microstructure from an underwater glider. *Methods Oceanogr.*, **10**, 44–69, https://doi.org/10.1016/j.mio.2014.05.002.

Polzin, K., 1996: Statistics of the Richardson number: Mixing models and finestructure. *J. Phys. Oceanogr.*, **26**, 1409–1425, https://doi.org/10.1175/1520-0485(1996)026%3C1409:SOTRNM%3E2.0.CO;2.

Polzin, K. L., J. M. Toole, and R. W. Schmitt, 1995: Finescale parameterizations of turbulent dissipation. *J. Phys. Oceanogr.*, **25**, 306–328, https://doi.org/10.1175/1520-0485(1995)025<0306:FPOTD>2.0.CO;2.

——, ——, J. R. Ledwell, and R. W. Schmitt, 1997: Spatial variability of turbulent mixing in the abyssal ocean. *Science*, **276**, 93–96, https://doi.org/10.1126/science.276.5309.93.

——, E. Kunze, J. Hummon, and E. Firing, 2002: The finescale response of lowered ADCP velocity profiles. *J. Atmos. Oceanic Technol.*, **19**, 205–224, https://doi.org/10.1175/1520-0426(2002)019<0205:TFROLA>2.0.CO;2.

——, A. C. Naveira Garabato, E. P. Abrahamsen, L. Jullion, and M. P. Meredith, 2014a: Boundary mixing in Orkney Passage outflow. *J. Geophys. Res. Oceans*, **119**, 8627–8645, https://doi.org/10.1002/2014JC010099.

——, ——, T. N. Huussen, B. M. Sloyan, and S. Waterman, 2014b: Finescale parameterizations of turbulent dissipation. *J. Geophys. Res. Oceans*, **119**, 1383–1419, https://doi.org/10.1002/2013JC008979.

Puthan, P., S. Sarkar, and G. Pawlak, 2021: Tidal synchronization of lee vortices in geophysical wakes. *Geophys. Res. Lett.*, **48**, e2020GL090905, https://doi.org/10.1029/2020GL090905.

Roget, E., I. Lozovatsky, X. Sanchez, and M. Figueroa, 2006: Microstructure measurements in natural waters: Methodology and applications. *Prog. Oceanogr.*, **70**, 126–148, https://doi.org/10.1016/j.pocean.2006.07.003.

Sanford, T. B., R. G. Drever, and J. H. Dunlap, 1978: A velocity profiler based on the principles of geomagnetic induction. *Deep-Sea Res.*, **25**, 183–210, https://doi.org/10.1016/0146-6291(78)90006-1.

Sanford, T., J. Dunlap, J. Carlson, D. Webb, and J. Girton, 2005: Autonomous velocity and density profiler: EM-APEX. *Proc. IEEE/OES Eighth Working Conf. on Current Measurement Technology*, Southampton, United Kingdom, IEEE, 152–156, https://doi.org/10.1109/CCM.2005.1506361.

Scott, R. B., and Y. Xu, 2009: An update on the wind power input to the surface geostrophic flow of the world ocean. *Deep-Sea Res. I*, **56**, 295–304, https://doi.org/10.1016/j.dsr.2008.09.010.

Sherman, J. T., and R. Pinkel, 1991: Estimates of the vertical wavenumber–frequency spectra of vertical shear and strain. *J. Phys. Oceanogr.*, **21**, 292–303, https://doi.org/10.1175/1520-0485(1991)021<0292:EOTVWS>2.0.CO;2.

Smyth, W. D., 2020: Marginal instability and the efficiency of ocean mixing. *J. Phys. Oceanogr.*, **50**, 2141–2150, https://doi.org/10.1175/JPO-D-20-0083.1.

Srinivasan, K., J. C. McWilliams, M. J. Molemaker, and R. O. Barkan, 2019: Submesoscale vortical wakes in the lee of topography. *J. Phys. Oceanogr.*, **49**, 1949–1971, https://doi.org/10.1175/JPO-D-18-0042.1.

——, ——, and A. Jagannathan, 2021: High vertical shear and dissipation in equatorial topographic wakes. *J. Phys. Oceanogr.*, **51**, 1985–2001, https://doi.org/10.1175/JPO-D-20-0119.1.

St. Laurent, L., S. Stringer, C. Garrett, and D. Perrault-Joncas, 2003: The generation of internal tides at abrupt topography. *Deep-Sea Res. I*, **50**, 987–1003, https://doi.org/10.1016/S0967-0637(03)00096-7.

Takahashi, T., and Coauthors, 2009: Climatological mean and decadal change in surface ocean pCO_2, and net sea–air CO_2 flux over the global oceans. *Deep-Sea Res. II*, **56**, 554–577, https://doi.org/10.1016/j.dsr2.2008.12.009.

Taylor, G. I., 1935: Statistical theory of turbulence. *Proc. Roy. Soc. London*, **151A**, 421–444, https://doi.org/10.1098/rspa.1935.0158.

Tennekes, H., and J. L. Lumley, 1972: *A First Course in Turbulence*. MIT Press, 320 pp.

Thomas, L. N., J. R. Taylor, R. Ferrari, and T. M. Joyce, 2013: Symmetric instability in the Gulf Stream. *Deep-Sea Res. II*, **91**, 96–110, https://doi.org/10.1016/j.dsr2.2013.02.025.

Thompson, R. O. R. Y., 1980: Efficiency of conversion of kinetic energy to potential energy by a breaking internal gravity wave. *J. Geophys. Res.*, **85**, 6631–6635, https://doi.org/10.1029/JC085iC11p06631.

Thomson, R. E., and W. J. Emery, 2014: Time series analysis methods. *Data Analysis Methods in Physical Oceanography*, 3rd ed. R. E. Thomson and W. J. Emery, Eds., Elsevier, 425–591.

Thorpe, S. A., 1973: Turbulence in stably stratified fluids: A review of laboratory experiments. *Bound.-Layer Meteor.*, **5**, 95–119, https://doi.org/10.1007/BF02188314.

——, 1992: The generation of internal waves by flow over the rough topography of a continental slope. *Proc. Roy. Soc. London*, **439A**, 115–130, https://doi.org/10.1098/rspa.1992.0137.

——, 2005: *The Turbulent Ocean*. Cambridge University Press, 484 pp.

Thurnherr, A. M., E. Kunze, J. M. Toole, L. St. Laurent, K. J. Richards, and A. Ruiz-Angulo, 2015: Vertical kinetic energy and turbulent dissipation in the ocean. *Geophys. Res. Lett.*, **42**, 7639–7647, https://doi.org/10.1002/2015GL065043.

Toole, J. M., R. W. Schmitt, K. L. Polzin, and E. Kunze, 1997: Near-boundary mixing above the flanks of a midlatitude seamount. *J. Geophys. Res.*, **102**, 947–959, https://doi.org/10.1029/96JC03160.

Trowbridge, J. H., and S. J. Lentz, 1991: Asymmetric behavior of an oceanic boundary layer above a sloping bottom. *J. Phys. Oceanogr.*, **21**, 1171–1185, https://doi.org/10.1175/1520-0485(1991)021<1171:ABOAOB>2.0.CO;2.

Tsutsumi, E., T. Matsuno, R.-C. Lien, H. Nakamura, T. Senjyu, and X. Guo, 2017: Turbulent mixing within the Kuroshio in the Tokara Strait. *J. Geophys. Res. Oceans*, **122**, 7082–7094, https://doi.org/10.1002/2017JC013049.

Waterman, S., A. C. Naveira Garabato, and K. L. Polzin, 2013: Internal waves and turbulence in the Antarctic circumpolar current. *J. Phys. Oceanogr.*, **43**, 259–282, https://doi.org/10.1175/JPO-D-11-0194.1.

——, K. L. Polzin, A. C. Naveira Garabato, K. L. Sheen, and A. Forryan, 2014: Suppression of internal wave breaking in the Antarctic circumpolar current near topography. *J. Phys. Oceanogr.*, **44**, 1466–1492, https://doi.org/10.1175/JPO-D-12-0154.1.

Whalen, C. B., L. D. Talley, and J. A. MacKinnon, 2012: Spatial and temporal variability of global ocean mixing inferred from Argo profiles. *Geophys. Res. Lett.*, **39**, L18612, https://doi.org/10.1029/2012GL053196.

——, J. A. MacKinnon, L. D. Talley, and A. F. Waterhouse, 2015: Estimating the mean diapycnal mixing using a finescale strain parameterization. *J. Phys. Oceanogr.*, **45**, 1174–1188, https://doi.org/10.1175/JPO-D-14-0167.1.

Wu, Y., E. Kunze, A. Tandon, and A. Mahadevan, 2023: Reabsorption of lee-wave energy in bottom-intensified currents. *J. Phys. Oceanogr.*, **53**, 477–491, https://doi.org/10.1175/JPO-D-22-0058.1.

Wunsch, C., and R. Ferrari, 2004: Vertical mixing, energy, and the general circulation of the oceans. *Annu. Rev. Fluid Mech.*, **36**, 281–314, https://doi.org/10.1146/annurev.fluid.36.%20050802.122121.

Zemskova, V. E., and N. Grisouard, 2021: Near-inertial dissipation due to stratified flow over abyssal topography. *J. Phys. Oceanogr*, **51**, 2483–2504, https://doi.org/10.1175/JPO-D-21-0007.1.

Zheng, K., and M. Nikurashin, 2019: Downstream propagation and remote dissipation of internal waves in the Southern Ocean. *J. Phys. Oceanogr.*, **49**, 1873–1887, https://doi.org/10.1175/JPO-D-18-0134.1.